# An Analytical Perspective on Bayesian Uncertainty Quantification and Propagation in Mode Shape Assembly

*Wang-Ji Yan[1,2*], Costas Papadimitriou[3], Lambros S. Katafygiotis[4], Dimitrios Chronopoulos[2]*

*[1] State Key Laboratory of Internet of Things for Smart City and Department of Civil and Environmental Engineering, University of Macau, China*
*[2]Institute for Aerospace Technology & The Composites Group, The University of Nottingham, United Kingdom*
*[3]Department of Mechanical and Industrial Engineering, University of Thessaly, Greece*
*[4]Department of Civil and Environmental Engineering, Hong Kong University of Science and Technology, Hong Kong, China*

**Abstract**: Assembling local mode shapes identified from multiple setups to form global mode shapes is of practical importance when the degrees of freedom (dofs) of interest are measured separately in individual setups or when one expects to exploit the computational autonomous capabilities of different setups in full-scale operational modal test. The Bayesian mode assembly methodology was able to obtain the optimal global mode shape as well as the associated uncertainties by taking the inverse of the analytically derived Hessian matrix of the negative log-likelihood function (NLLF) [1]. In this study, we investigate how the posterior uncertainties existing in the local mode shapes obtained from different setups propagate into the global mode shapes in an explicit manner by borrowing a novel approximate analysis strategy. The explicit closed-form approximation expressions are derived to investigate the effects of various data parameters on the posterior covariance matrix of the global mode shapes. Such quantitative relationships, connecting the posterior uncertainties with global mode shapes and the data information, offer a better understanding of uncertainty propagation over the process of mode shape assembly. The posterior uncertainty of the global mode shapes is inversely proportional to ‘normalized data length’ and the ‘frequency bandwidth factor’, and propositional to ‘noise-to-environment’ ratio and damping ratio. Validation studies using field test data measured from the Metsovo bridge located in Greece provide a practical verification of the rationality of the theoretical findings of uncertainty quantification and propagation analysis in Bayesian mode shape assembly.

**Keywords:** Operational modal analysis; Mode shape assembly; Bayesian analysis; Uncertainty propagation; Approximation analysis

---

*Corresponding author.
E-mail address: civilyanwj@gmail.com (W.J. Yan); costasp@uth.gr (C. Papadimitriou); katafygiotis.lambros@gmail.com (L. Katafygiotis ); ezzdc@exmail.nottingham.ac.uk (D. Chronopoulos)

## 1 Introduction

Operational modal analysis (OMA) which primarily identifies the natural frequencies, damping ratios and mode shapes has gained increasing popularity in both theoretical developments and practical applications. In full-scale operational modal tests, assembling mode shapes identified from multiple setups often arises due to a number of practical reasons [1-3] shown as follows:

- The degrees of freedom (dofs) of interest are often measured separately as the number of sensors available is usually not adequate to cover the entire structure in one setup under a limited instrumentation budget.
- The amount of data acquired may be too large to be processed simultaneously in a single setup even when the number of sensors available is large enough for modal testing, which poses challenges for computers with limited memory space or computation capacity.
- One can exploit the computational autonomous capabilities of wireless sensor network by a distributed computing strategy in full-scale operational modal test. The wireless sensors are usually divided into several communities with each community composed of a cluster head node and several leaf nodes. Each cluster processes partial mode shape information corresponding to the dofs of the cluster nodes.

In all these cases, the dofs of interest are usually divided into several sensor setups with common 'reference' dofs present across different setups. The acquired data for each setup is usually processed individually. Usually, one shares only a single fixed reference sensor across any two setups, whose mode shape component is then normalized to unit [4,5]. However, in many cases, no fixed reference dofs are shared by all setups. Worse still, more than one reference dof is required when the reference dof lacks modal contribution in some particular modes. Therefore, it is challenging to assemble a group of local mode shapes which share more than one reference sensors or share unfixed references sensors.

When addressing the issue of mode shape assembly, uncertainties existing in the local mode shapes stemming from measurement noise and modelling error will inevitably propagate into the assembled global mode shapes. The assessment and study of the uncertainty or variability has now been widely recognized as an important consideration in OMA [6-8]. A number of statistical approaches have been developed to quantify the uncertainty of OMA over the past decades [9-15]. Prominent references of statistical approaches include the development of frequency-domain maximum likelihood (ML) techniques [9-11] and stochastic subspace identification (SSI) based methods [12-15]. Bayesian statistics is considered to be another promising approach for uncertainty quantification as it views probability as a multi-valued propositional logic for plausible reasoning [16]. Beck and Katafygiotis proposed a Bayesian system identification framework [17], which lead to an increase in interest in the application of Bayesian statistics in various fields of structural dynamics, including structural model updating [18-22], damage detection [23], reliability updating [24,25], model selection [26,27], etc.

Bayesian statistics has also played an important role in addressing the problem of OMA driven by the statistics of time histories, FFT, PSD, and transmissibility function [28-40]. In the field of OMA, the first-generation Bayesian OMA approaches in the time domain and frequency domain were proposed by Yuen and Katafygiotis [28-30]. These works lay a mathematically rigorous theoretical foundation for OMA accommodating multiple uncertainties. Unfortunately, the original formulations suffer from some computational problems. More recently, the second-generation Bayesian OMA approaches have been proposed due to a novel contribution made by Au [31,32] through employing advanced mathematical techniques to address the computational challenges of the conventional Bayesian FFT approach [28]. The fast Bayesian OMA method has been successfully applied to a number of engineering structures. However, the work on uncertainty analysis for mode shape assembly is still relatively rare. Uncertainty quantification and propagation for global mode shapes has remained an important problem worth of further investigation in the field of OMA.

Inspired by the 'global least squares approach' [2] which has great advantages over the 'local least squares method', a Bayesian algorithm that has no need to share the same set of reference dofs in order to obtain proper scaling to form the overall mode shapes was proposed in [1]. The proposed algorithm is able to account for the weight for different setups properly, according to the various setups' data quality. The probability distributions of the global mode shapes are updated from their initial prior distribution to the posterior distribution given the measured data and modelling assumptions. The most probable global mode shapes are represented by the peaks of the posterior distribution, while their posterior uncertainties are provided by the spread of the distribution around the most probable values (MPV).

In [1], the covariance matrix of the global mode shapes can be obtained by directly taking the inverse of the Hessian matrix using numerical methods. However, such implicit numerical implementation does not allow one to investigate intrinsic uncertainty propagation properties [38,39]. For example, it is highly non-trivial to identify how different data parameters (e.g., data duration, the number of data segments or the spectral bandwidth) will affect the overall uncertainty of the assembled global mode shapes. To realize the aforementioned objective, it is natural for one to seek a deeper understanding of the process of uncertainty propagation in mode shape assembly problem by resorting to an analytic solution.

By employing an innovative approximation analysis strategy, explicit closed-form approximation of the posterior uncertainty of the local mode shape corresponding to a single setup have been derived analytically in the case of well-separated modes, small damping and sufficient data in [38,39]. Making full use of the work on uncertainty law of ambient modal identification [38,39], the primary focus of this paper is to further analytically derive explicit expressions for the approximated covariance matrix of the assembled global mode shapes in terms of different data parameters. The derived expressions are insightful, indicating how the posterior uncertainties of the local mode shapes quantified by using fast Bayesian FFT approach confined to different setups propagate into the assembled global mode shapes in an explicit manner. The implications of these results are also investigated and verified with simulated data and field test data.

This paper is organized as follows: For the sake of completeness, the general formulation of the Bayesian mode shape assembly algorithm [1] is briefly reviewed in section 2. In section

3, the approximate posterior covariance matrix of the global mode shapes is derived analytically under asymptotic conditions. In section 4 and section 5, the theories are verified using simulated data of a 2-D shear building and the field test data of the Metsovo bridge located in Greece.

## 2 Bayesian Uncertainty Quantification for Mode Shape Assembly

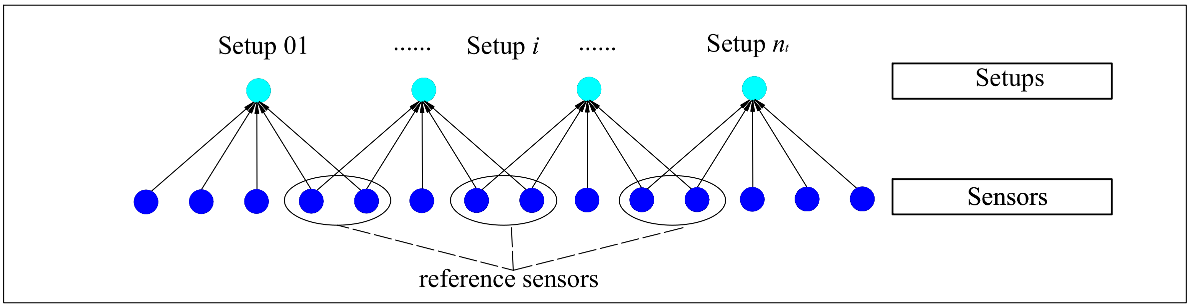


Fig. 1: Common architecture for operational modal test with multiple setups

As shown in Fig. 1, the dofs of interest are divided into several groups which are measured separately with common 'reference' dofs present across different setups. It is assumed that there are $n_t$ setups included in the ambient vibration test, and the number of sensors measured in the $i$-th setup is $n_i$. The total number of distinct measured dofs from all setups is denoted by $n_l$, where $n_l < 1+\sum_{i=1}^{n_t}(n_i\text{-}1)=1\text{-}n_t+\sum_{i=1}^{n_t} n_i$ since at least one dof in each setup is shared by at least another setup. For each setup, the modal properties can be identified by utilizing Bayesian approaches such as fast Bayesian FFT approach [31]. Suppose that $f_{r,i}$ (modal frequency), $\varsigma_{r,i}$ (modal damping ratio), $\mathrm{S}_{f,r,i}$ ( Power Spectral Density (PSD) of modal excitation) and $s_{\mu,r,i}$ (PSD of prediction error) denote the spectrum variables of the $r$-th mode identified using the data information of the $i$-th setup only, while $\hat{\boldsymbol{\psi}}_{r,i} \in \mathbb{R}^{n_i}$ and

$\mathbf{C}_{\psi_{r,i}} \in \mathbb{R}^{n_i \times n_i}$ denote the optimal values and covariance matrix of the $r$-th local mode shape confined to the measured dofs of the $i$-th setup $(i = 1, 2, \cdots, n_t)$.

### *2.1 Basic formulation of Bayesian mode shape assembly algorithm*

The mode shape assembly problem amounts to determining the global mode shapes that best fit the identified local counterparts. Let $\boldsymbol{\varphi}_r \in \mathbb{R}^{n_l}$ be the $r$-th global mode shape covering all measured dofs which are required to be identified, while $\boldsymbol{\varphi}_{r,i} \in \mathbb{R}^{n_i}$ be the components of $\boldsymbol{\varphi}_r$ confined to the measured dofs in the $i$-th setup. The local mode shape $\boldsymbol{\varphi}_{r,i}$ can be mathematically related to the global mode shape $\boldsymbol{\varphi}_r$ as [2]

$$\boldsymbol{\varphi}_{r,i} = \mathbf{L}_i \boldsymbol{\varphi}_r \tag{1}$$

where $\mathbf{L}_i \in \mathbb{R}^{n_i \times n_l}$ is a selection matrix, with elements $\mathbf{L}_i(p,q) = 1$ if the $p$-th sensor of the $i$-th setup corresponds to the $q$-th dof of $\boldsymbol{\varphi}_r$ and zero otherwise.

It is worth noting that $\hat{\boldsymbol{\psi}}_{r,i}$ identified using Bayesian approach [31] is normalized to unity. Therefore, the measure-of-fit should be implemented based on the discrepancy between $\boldsymbol{\varphi}_{r,i} / \|\boldsymbol{\varphi}_{r,i}\|$ and $\hat{\boldsymbol{\psi}}_{r,i}$, both have been subjected to similar normalization involving unit norms. Since the $i$-th local mode shape $\hat{\boldsymbol{\psi}}_{r,i}$ can be well-approximated by a Gaussian distribution, the likelihood function $p(\hat{\boldsymbol{\psi}}_{r,i}, \mathbf{C}_{\psi_{r,i}} | \boldsymbol{\varphi}_{r,i})$ expressing the contribution of $(\hat{\boldsymbol{\psi}}_{r,i}, \mathbf{C}_{\psi_{r,i}})$ is given by

$$p(\hat{\boldsymbol{\psi}}_{r,i}, \mathbf{C}_{\psi_{r,i}} | \boldsymbol{\varphi}_{r,i}) = \exp[-\frac{1}{2}(\boldsymbol{\varphi}_{r,i} / \|\boldsymbol{\varphi}_{r,i}\| - \hat{\boldsymbol{\psi}}_{r,i})^T (\mathbf{C}_{\psi_{r,i}}^{-1})(\boldsymbol{\varphi}_{r,i} / \|\boldsymbol{\varphi}_{r,i}\| - \hat{\boldsymbol{\psi}}_{r,i})] \tag{2}$$

As vibration testing for different setups are conducted independently and data sets are independently collected, it is reasonable to assume that local mode shapes identified from different setups are statistically independent, then the updated probability of the global mode shape given the measured local mode shapes $\wp$ satisfies:

$$p(\boldsymbol{\varphi}_r|\wp) = c_0 p(\boldsymbol{\varphi}_r) p(\wp|\boldsymbol{\varphi}_r) = c_0 p(\boldsymbol{\varphi}_r) \prod_{i=1}^{n_t} p(\hat{\boldsymbol{\psi}}_{r,i}, \mathbf{C}_{\boldsymbol{\psi}_{r,i}} |\boldsymbol{\varphi}_{r,i}) \tag{3}$$

In the case where a non-informative prior is used, $p(\boldsymbol{\varphi}_r|\wp)$ can be written in terms of the 'negative log-likelihood function' (NLLF) as $p(\boldsymbol{\varphi}_r|\wp) \propto \exp(-L_{as}(\boldsymbol{\varphi}_r))$ with

$$L_{as} = \frac{1}{2}\sum_{i=1}^{n_t}\left(\mathbf{L}_i\boldsymbol{\varphi}_r / \|\mathbf{L}_i\boldsymbol{\varphi}_r\| - \hat{\boldsymbol{\psi}}_{r,i}\right)^T (\mathbf{C}_{\boldsymbol{\psi}_{r,i}}^{-1})\left(\mathbf{L}_i\boldsymbol{\varphi}_r / \|\mathbf{L}_i\boldsymbol{\varphi}_r\| - \hat{\boldsymbol{\psi}}_{r,i}\right) \tag{4}$$

The above equation is subject to the constraint of $\boldsymbol{\varphi}_r^T\boldsymbol{\varphi}_r=1$. Determining the optimal $\boldsymbol{\varphi}_r$ involves the minimization of (4) subject to the constraint of $\boldsymbol{\varphi}_r^T\boldsymbol{\varphi}_r=1$, which is not quadratic with respect to $\boldsymbol{\varphi}_r$. To avoid this computational difficulty, the objective function can be reformulated as [1],

$$L'_{as} = \sum_{i=1}^{n_t}\frac{1}{2}(\chi_{r,i}\mathbf{L}_i\boldsymbol{\varphi}_r - \hat{\boldsymbol{\psi}}_{r,i})^T(\mathbf{C}_{\boldsymbol{\psi}_{r,i}}^{-1})(\chi_{r,i}\mathbf{L}_i\boldsymbol{\varphi}_r - \hat{\boldsymbol{\psi}}_{r,i}) + \gamma_r(1-\boldsymbol{\varphi}_r^T\boldsymbol{\varphi}_r) + \sum_{i=1}^{n_t}\beta_{r,i}(\chi_{r,i}^2\|\mathbf{L}_i\boldsymbol{\varphi}_r\|^2 - 1) \tag{5}$$

where the auxiliary variables $\chi_{r,i}^2$ and $\beta_{r,i}$ denote Lagrange multipliers that enforce $\chi_{r,i}^2 = 1/\|\mathbf{L}_i\boldsymbol{\varphi}_r\|^2$ ; $\gamma_r$ is Lagrange multiplier that enforce the unit norm condition $\|\boldsymbol{\varphi}_r\|=1$. The full set of parameters to be identified is $\boldsymbol{\lambda}_{as} = \{\boldsymbol{\varphi}_r, \gamma_r, \beta_{r,i}, \chi_{r,i} : i = 1,2\cdots,n_t\}$.

### *2.2 MPVs of the global mode shapes*

Sharing some common features with the 'global least squares method', the minimization problem (5) can be solved by an iterative solution strategy to address the difficulties stemming from the high-dimensional and nonlinear nature of the problem. The initial guess of the global mode shapes is taken as the eigenvector (with unit norm) of $\boldsymbol{\Theta}$ with the smallest eigenvalue [3,4]

$$\mathbf{\Theta} = \sum_{i=1}^{n_i} \mathbf{L}_i^T \left( \left( \hat{\boldsymbol{\psi}}_{r,i}^T \mathbf{D}_i \hat{\boldsymbol{\psi}}_{r,i} \right) \mathbf{I}_{n_i} - \mathbf{D}_i \right) \mathbf{L}_i \tag{6}$$

where $\mathbf{D}_i$ is the sum of PSD matrices over all frequencies in the selected band in setup $i$. Given the initial guess of the global mode shapes, a sequence of iterations comprised of the following linear optimization problems can be implemented to solve the Bayesian mode shape assembly problem. Instead of optimizing the full set of parameters simultaneously, the optimal parameters can be optimized in two groups, one group at a time assuming fixed values for the parameters in all remaining groups, until convergence is reached [1]:

**(1) Optimal $\chi_{r,i}$ and $\beta_{r,i}$**

The optimal values of $\chi_{r,i}$ and $\beta_{r,i}$ in terms of $\boldsymbol{\varphi}_r$ and $\gamma_r$ are firstly derived analytically:

$$\hat{\beta}_{r,i} = -\frac{(\mathbf{L}_i \boldsymbol{\varphi}_r)^T \mathbf{C}_{\psi_{r,i}}^{-1} \mathbf{L}_i \boldsymbol{\varphi}_r}{2\left\| \mathbf{L}_i \boldsymbol{\varphi}_r \right\|^2} + \left| \frac{\hat{\boldsymbol{\psi}}_{r,i}^T \mathbf{C}_{\psi_{r,i}}^{-1} \mathbf{L}_i \boldsymbol{\varphi}_r}{2\left\| \mathbf{L}_i \boldsymbol{\varphi}_r \right\|} \right| \tag{7a}$$

$$\hat{\chi}_{r,i} = \frac{\hat{\boldsymbol{\psi}}_{r,i}^T \mathbf{C}_{\psi_{r,i}}^{-1} (\mathbf{L}_i \boldsymbol{\varphi}_r)}{\left| \hat{\boldsymbol{\psi}}_{r,i}^T \mathbf{C}_{\psi_{r,i}}^{-1} \mathbf{L}_i \boldsymbol{\varphi}_r \left\| \mathbf{L}_i \boldsymbol{\varphi}_r \right\| \right|} = \operatorname{sgn}(\hat{\boldsymbol{\psi}}_{r,i}^T \mathbf{C}_{\psi_{r,i}}^{-1} \mathbf{L}_i \boldsymbol{\varphi}_r) \left\| \mathbf{L}_i \boldsymbol{\varphi}_r \right\|^{-1} \tag{7b}$$

where $\operatorname{sgn}(\cdot)$ denotes the signum function.

**(2) Optimal $\boldsymbol{\varphi}_r$ and $\gamma_r$**

The global mode shape $\boldsymbol{\varphi}_r$ and the auxiliary variable $\gamma_r$ can be solved using the following constrained equation [1]:

$$\mathbf{A}_r \boldsymbol{\varphi}_r + \mathbf{b}_r = \gamma_r \boldsymbol{\varphi}_r \tag{8}$$

where $\mathrm{A}_r = \frac{1}{2}\sum_{i=1}^{n_t} \chi_{r,i}^2 \mathbf{L}_i^T \mathbf{C}_{\psi_{r,i}}^{-1} \mathbf{L}_i + \sum_{i=1}^{n_t} \beta_{r,i} \chi_{r,i}^2 \mathbf{L}_i^T \mathbf{L}_i$ and $b_r = -\frac{1}{2}\sum_{i=1}^{n_t} \chi_{r,i} \mathbf{L}_i^T \mathbf{C}_{\psi_{r,i}}^{-1} \hat{\boldsymbol{\psi}}_{r,i}$. Eq. (8) accompanied by the constraint $\left\| \boldsymbol{\varphi}_r \right\|^2 = 1$ form a constrained eigenvalue problem, which can be solved by constructing an augmented vector satisfying the standard eigenvalue equation [2]:

$$\Lambda \mathbf{z} = \gamma_r \mathbf{z} \tag{9}$$

where $\Lambda = \begin{bmatrix} \mathbf{A}_r & \mathbf{b}_r\mathbf{b}_r^T \\ \mathbf{I}_{n_t} & \mathbf{A}_r \end{bmatrix}$ and $z = \{\boldsymbol{\varphi}_r \quad \mathbf{y}\}^T \in \Re^{2\times n_t}$ with $\mathbf{y}$ being an auxiliary vector. The first $n_t$ components of the vector $z = \{\boldsymbol{\varphi}_r \quad \mathbf{y}\}^T \in \Re^{2\times n_t}$ just correspond to the MPVs of the global mode shapes $\hat{\boldsymbol{\varphi}}_r$.

### *2.3 Posterior covariance matrix of the global mode shapes*

The posterior distribution of $\boldsymbol{\varphi}_r$ can be well approximated by a multivariate Gaussian distribution centered at the MPVs $\hat{\boldsymbol{\varphi}}_r$. The posterior uncertainty of the global mode shape can be obtained by inverting the Hessian matrix of NLLF calculated at the optimal values $\hat{\boldsymbol{\varphi}}_r$. In the original formulation of the algorithm [1], the Hessian matrix of the modified NLLF $L'_{as}$ with respect to the global mode shapes and the auxiliary variables involved in (5) is employed for calculating the uncertainties of global mode shape. However, the Hessian matrix with respect to $\boldsymbol{\lambda}_{as} = \{\boldsymbol{\varphi}_r, \gamma_r, \beta_{r,i}, \chi_{r,i} : i = 1,2\cdots,n_t\}$ is vulnerable to suffering from singularity. It is more accurate to calculate the uncertainties of $\boldsymbol{\varphi}_r$ using the original NLLF of (4) which is invariant to the constraint of $\boldsymbol{\varphi}_r$:

$$\begin{aligned} L_{as} &= \frac{1}{2}\sum_{i=1}^{n_t}\left( \mathbf{L}_i \frac{\boldsymbol{\varphi}_r}{\|\boldsymbol{\varphi}_r\|} \bigg/ \left\| \mathbf{L}_i \frac{\boldsymbol{\varphi}_r}{\|\boldsymbol{\varphi}_r\|} \right\| - \hat{\boldsymbol{\psi}}_{r,i} \right)^T (\mathbf{C}_{\psi_{r,i}}^{-1}) \left( \mathbf{L}_i \frac{\boldsymbol{\varphi}_r}{\|\boldsymbol{\varphi}_r\|} \bigg/ \left\| \mathbf{L}_i \frac{\boldsymbol{\varphi}_r}{\|\boldsymbol{\varphi}_r\|} \right\| - \hat{\boldsymbol{\psi}}_{r,i} \right) \\ &= \frac{1}{2}\sum_{i=1}^{n_t} \left( \mathbf{L}_i\boldsymbol{\varphi}_r / \|\mathbf{L}_i\boldsymbol{\varphi}_r\| - \hat{\boldsymbol{\psi}}_{r,i} \right)^T \mathbf{C}_{\psi_{r,i}}^{-1} \left( \mathbf{L}_i\boldsymbol{\varphi}_r / \|\mathbf{L}_i\boldsymbol{\varphi}_r\| - \hat{\boldsymbol{\psi}}_{r,i} \right) \end{aligned} \tag{10}$$

According to the derivation shown in Appendix I, the Hessian matrix of (10) with respect to $\boldsymbol{\varphi}_r$ can be obtained as:

$$L_{as}^{(\boldsymbol{\varphi}_r\boldsymbol{\varphi}_r)} = \sum_{i=1}^{n_t}\left[\left(\boldsymbol{\varphi}_r^T\mathbf{B}_i\boldsymbol{\varphi}_r\right)^{-3}\left\{\begin{array}{l}\left(\boldsymbol{\varphi}_r^T\mathbf{B}_i\boldsymbol{\varphi}_r\right)\left[-\left(\boldsymbol{\varphi}_r^T\mathbf{A}_{r,i}\boldsymbol{\varphi}_r\right)\mathbf{B}_i - 4\left(\mathbf{B}_i\boldsymbol{\varphi}_r\right)\left(\boldsymbol{\varphi}_r^T\mathbf{A}_{r,i}\right)\right]+\left(\boldsymbol{\varphi}_r^T\mathbf{B}_i\boldsymbol{\varphi}_r\right)^2\mathbf{A}_{r,i}+\\ 4\left(\boldsymbol{\varphi}_r^T\mathbf{A}_{r,i}\boldsymbol{\varphi}_r\right)\left(\mathbf{B}_i\boldsymbol{\varphi}_r\boldsymbol{\varphi}_r^T\mathbf{B}_i\right)+\left(\boldsymbol{\varphi}_r^T\mathbf{B}_i\boldsymbol{\varphi}_r\right)^{3/2}\left[\left(\boldsymbol{\eta}_{r,i}^T\boldsymbol{\varphi}_r\right)\mathbf{B}_i+2\left(\mathbf{B}_i\boldsymbol{\varphi}_r\boldsymbol{\eta}_{r,i}^T\right)\right]\\ -3\left(\boldsymbol{\varphi}_r^T\mathbf{B}_i\boldsymbol{\varphi}_r\right)^{1/2}\left(\boldsymbol{\eta}_{r,i}^T\boldsymbol{\varphi}_r\right)\left(\mathbf{B}_i\boldsymbol{\varphi}_r\boldsymbol{\varphi}_r^T\mathbf{B}_i\right)\end{array}\right\}\right] \quad (11)$$

where $L_{as}^{(\boldsymbol{\varphi}_r\boldsymbol{\varphi}_r)}$ denotes the Hessian matrix and

$$\mathbf{A}_{r,i} = \mathbf{L}_i^T\mathbf{C}_{\boldsymbol{\psi}_{r,i}}^{-1}\mathbf{L}_i \quad (12a)$$

$$\mathbf{B}_i = \mathbf{L}_i^T\mathbf{L}_i \quad (12b)$$

$$\boldsymbol{\eta}_{r,i}^T = \hat{\boldsymbol{\psi}}_{r,i}^T\mathbf{C}_{\boldsymbol{\psi}_{r,i}}^{-1}\mathbf{L}_i \quad (12c)$$

As a result, the posterior covariance of the assembled overall mode shapes can be computed by taking the inverse of (11).

It is worth noting that the NLLF (10) is invariant to the scaling of $\boldsymbol{\varphi}_r$, and the Hessian of NLLF has a zero eigenvalue with eigenvector $\boldsymbol{\varphi}_r$. Therefore, similar to [3], we have to exclude the irrelevant contributions from the singular terms (zero curvature) when taking the inverse of $L_{as}^{(\boldsymbol{\varphi}_r\boldsymbol{\varphi}_r)}$. Let $\{\xi_1',\xi_2',\cdots,\xi_{n_l}'\}$ be the eigenvalues of $L_{as}^{(\boldsymbol{\varphi}_r\boldsymbol{\varphi}_r)}$ in ascending order, while the corresponding eigenvectors are assumed to be $\{\boldsymbol{\upsilon}_1',\boldsymbol{\upsilon}_2',\cdots,\boldsymbol{\upsilon}_{n_l}'\}$. The covariance matrix $\mathbf{C}_{\boldsymbol{\varphi}_r}$ can be evaluated properly via its eigen-basis representation with the first smallest eigenvalue ignored:

$$\mathbf{C}_{\boldsymbol{\varphi}_r} = \sum_{j=2}^{n_l}\xi_j'^{-1}\boldsymbol{\upsilon}_j'\boldsymbol{\upsilon}_j'^T \quad (13)$$

## 3 Uncertainty Propagation Properties in Mode Shape Assembly

### *3.1 Approximate covariance matrix of the local mode shapes*

It is worth recalling here that that $f_{r,i}$, $\varsigma_{r,i}$, $S_{f,r,i}$, $s_{\mu,r,i}$, $\hat{\boldsymbol{\psi}}_{r,i} \in \mathbb{R}^{n_i}$ and $\mathbf{C}_{\boldsymbol{\psi}_{r,i}} \in \mathbb{R}^{n_i\times n_i}$ denote modal frequency, modal damping ratio PSD of modal excitation, PSD of prediction error, the optimal values and covariance matrix of the $r$-th local mode shape confined to the measured dofs of the $i$-th setup $(i=1,2,\cdots,n_t)$. For the $r$-th mode of $i$-th setup, assume that the frequency band selected for analysis is $2\kappa\varsigma_{r,i}f_{r,i}$ (i.e., $f_s\left(1\pm\kappa\varsigma_{r,i}\right)$), with $\kappa$ being defined as the 'bandwidth factor' [38,39]. As a result, the number of FFT ordinates contained in the selected frequency band is equal to [38,39]

$$N_f=\text{Int}\left(\frac{2\kappa\varsigma_{r,i}f_{r,i}}{1/\left(N_{c,r,i}T_n\right)}\right)=\text{Int}\left(2\kappa\varsigma_{r,i}N_{c,r,i}\right) \tag{14}$$

where $\text{Int}(\cdot)$ denote round number to make sure that $N_f$ be an integer; $N_{c,r,i}$ denotes the 'normalized data length' which should satisfy $N_{c,r,i}=\dfrac{T_d}{T_{n,r,i}}\gg 1$ with $T_{n,r,i}=1/f_{r,i}$ and $T_d$ denoting the natural period and data duration, respectively.

Given the conditions that the damping ratio $\varsigma_{r,i}$ for the structure is assumed to be small, the 'noise-to-signal ratio' $\nu_{r,i}=s_{\mu,r,i}/S_{f,r,i}$ is small, and the data duration $T_d$ is assumed to be long, it has been proved that the Hessian matrix and the posterior covariance matrix to the leading order for the $i$-th local mode shapes identified using Bayesian FFT approach is given by [38,39]:

$$L^{(\psi_{r,i}\psi_{r,i})}=\left[\mathbf{C}_{\psi_{r,i}}\right]^{-1}\approx\frac{N_{c,r,i}\tan^{-1}\kappa}{\nu_{r,i}\varsigma_{r,i}}\left(\mathbf{I}_{n_i}-\hat{\boldsymbol{\psi}}_{r,i}\hat{\boldsymbol{\psi}}_{r,i}^T\right) \tag{15a}$$

$$\mathbf{C}_{\psi_{r,i}}\approx\frac{\nu_{r,i}\varsigma_{r,i}}{N_{c,r,i}\tan^{-1}\kappa}\left(\mathbf{I}_{n_i}-\hat{\boldsymbol{\psi}}_{r,i}\hat{\boldsymbol{\psi}}_{r,i}^T\right) \tag{15b}$$

where $\nu_{r,i}=s_{\mu,r,i}/S_{f,r,i}$ denotes 'noise-to-signal ratio' confined to $i$-th the setup. The data length factor $\tan^{-1}\kappa$ is shown in Fig. 2, which indicate the variation of the data length factors with the increase of bandwidth factor. From Fig. 2, one can figure out that the bandwidth factor converges to stable values quickly.

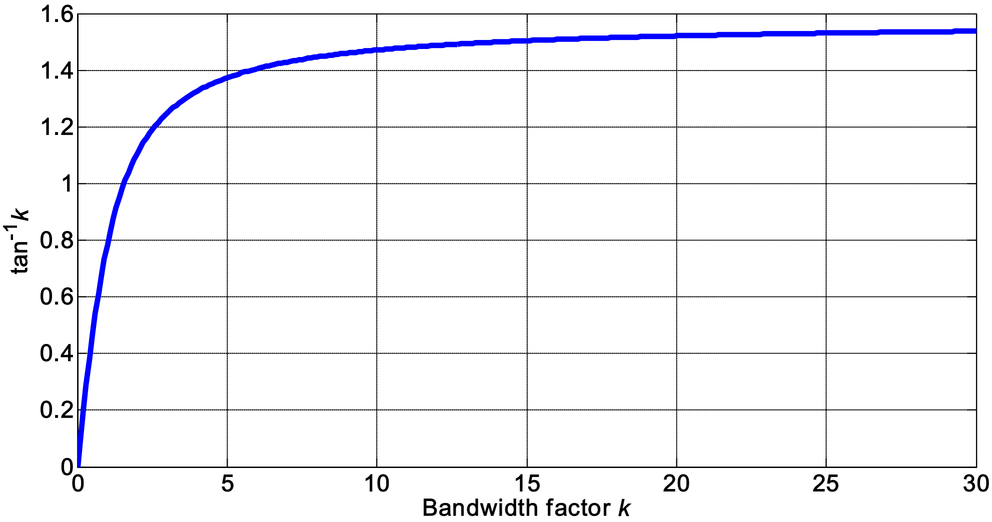


Fig. 2: The data length factor for the local mode shape

***3.2 Approximated Hessian matrix of the Bayesian mode shape assembly algorithm***

The Hessian matrix shown in (11) is a linear combination of $n_t$ terms with each term given by a complicated expression. The target of this section is to derive an explicit approximate expression of the posterior covariance matrix of the global mode shapes based on the asymptotic expressions (15a) and (15b) for the Hessian and covariance matrices of $i$-th local mode shape. By substituting (15a) into (12c) and using the normalization condition that $\hat{\boldsymbol{\psi}}_{r,i}^T \hat{\boldsymbol{\psi}}_{r,i} = 1$, one can obtain that

$$
\begin{aligned}
\boldsymbol{\eta}_{r,i}^{T} &= \hat{\boldsymbol{\psi}}_{r,i}^{T}\mathbf{C}_{\psi_{r,i}}^{-1}\mathbf{L}_{i} \\
&\approx \frac{N_{c,r,i}\tan^{-1}\kappa}{\nu_{r,i}\varsigma_{r,i}}\left[\hat{\boldsymbol{\psi}}_{r,i}^{T}\left(\mathbf{I}_{n_i}-\hat{\boldsymbol{\psi}}_{r,i}\hat{\boldsymbol{\psi}}_{r,i}^{T}\right)\mathbf{L}_{i}\right]^{T} \\
&= \frac{N_{c,r,i}\tan^{-1}\kappa}{\nu_{r,i}\varsigma_{r,i}}\left[\hat{\boldsymbol{\psi}}_{r,i}^{T}\mathbf{L}_{i}-\left(\hat{\boldsymbol{\psi}}_{r,i}^{T}\hat{\boldsymbol{\psi}}_{r,i}\right)\hat{\boldsymbol{\psi}}_{r,i}^{T}\mathbf{L}_{i}\right]^{T} \\
&= \frac{N_{c,r,i}\tan^{-1}\kappa}{\nu_{r,i}\varsigma_{r,i}}\left(\hat{\boldsymbol{\psi}}_{r,i}^{T}\mathbf{L}_{i}-\hat{\boldsymbol{\psi}}_{r,i}^{T}\mathbf{L}_{i}\right)^{T} \\
&= \mathbf{0}
\end{aligned} \tag{16}
$$

Substituting (15a) into (12a) leads to

$$
\begin{aligned}
\mathbf{A}_{r,i} &= \mathbf{L}_{i}^{T}\mathbf{C}_{\psi_{r,i}}^{-1}\mathbf{L}_{i} \\
&\approx \frac{N_{c,r,i}\tan^{-1}\kappa}{\nu_{r,i}\varsigma_{r,i}}\mathbf{L}_{i}^{T}\left(\mathbf{I}_{n_i}-\hat{\boldsymbol{\psi}}_{r,i}\hat{\boldsymbol{\psi}}_{r,i}^{T}\right)\mathbf{L}_{i} \\
&= \frac{N_{c,r,i}\tan^{-1}\kappa}{\nu_{r,i}\varsigma_{r,i}}\left[\mathbf{B}_{i}-\mathbf{L}_{i}^{T}\hat{\boldsymbol{\psi}}_{r,i}\hat{\boldsymbol{\psi}}_{r,i}^{T}\mathbf{L}_{i}\right]
\end{aligned} \tag{17}
$$

Under the assumption of well-separated modes with high 'signal-to-noise ratio', $\hat{\boldsymbol{\psi}}_{r,i}$ can be approximated using the counterpart of assembled global mode shapes:

$$
\hat{\boldsymbol{\psi}}_{r,i} \approx \left\|\mathbf{L}_{i}\boldsymbol{\varphi}_{r}\right\|^{-1}\mathbf{L}_{i}\boldsymbol{\varphi}_{r} \tag{18}
$$

Therefore, (17) can be further rearranged as

$$
\mathbf{A}_{r,i} \approx \frac{N_{c,r,i}\tan^{-1}\kappa}{\nu_{r,i}\varsigma_{r,i}}\left(\mathbf{B}_{i}-\left\|\mathbf{L}_{i}\boldsymbol{\varphi}_{r}\right\|^{-2}\mathbf{L}_{i}^{T}\mathbf{L}_{i}\boldsymbol{\varphi}_{r}\boldsymbol{\varphi}_{r}^{T}\mathbf{L}_{i}^{T}\mathbf{L}_{i}\right) \approx \frac{N_{c,r,i}\tan^{-1}\kappa}{\nu_{r,i}\varsigma_{r,i}}\boldsymbol{\Omega}_{i} \tag{19}
$$

where

$$
\boldsymbol{\Omega}_{i} = \left[\mathbf{B}_{i}-\mathbf{B}_{i}\boldsymbol{\varphi}_{r}\boldsymbol{\varphi}_{r}^{T}\mathbf{B}_{i}\big/\left(\boldsymbol{\varphi}_{r}^{T}\mathbf{B}_{i}\boldsymbol{\varphi}_{r}\right)\right] \tag{20}
$$

Substituting (16) and (19) into (11) results in

$$
L_{as}^{(\varphi_r\varphi_r)} \approx \tilde{L}_{as}^{(\varphi_r\varphi_r)} = \sum_{i=1}^{n_t}\left[\frac{N_{c,r,i}\tan^{-1}\kappa}{\nu_{r,i}\varsigma_{r,i}}\left(\boldsymbol{\varphi}_{r}^{T}\mathbf{B}_{i}\boldsymbol{\varphi}_{r}\right)^{-3}\left\{\begin{array}{l}-\left(\boldsymbol{\varphi}_{r}^{T}\mathbf{B}_{i}\boldsymbol{\varphi}_{r}\right)\left(\boldsymbol{\varphi}_{r}^{T}\boldsymbol{\Omega}_{i}\boldsymbol{\varphi}_{r}\right)\mathbf{B}_{i}+\left(\boldsymbol{\varphi}_{r}^{T}\mathbf{B}_{i}\boldsymbol{\varphi}_{r}\right)^{2}\boldsymbol{\Omega}_{i}+ \\ 4\left(\boldsymbol{\varphi}_{r}^{T}\boldsymbol{\Omega}_{i}\boldsymbol{\varphi}_{r}\right)\left(\mathbf{B}_{i}\boldsymbol{\varphi}_{r}\boldsymbol{\varphi}_{r}^{T}\mathbf{B}_{i}\right)-4\left(\boldsymbol{\varphi}_{r}^{T}\mathbf{B}_{i}\boldsymbol{\varphi}_{r}\right)\left(\mathbf{B}_{i}\boldsymbol{\varphi}_{r}\boldsymbol{\varphi}_{r}^{T}\boldsymbol{\Omega}_{i}\right)\end{array}\right\}\right] \tag{21}
$$

Substituting $\boldsymbol{\Omega}_{i}$ from (20) and noting that inside the bracket in (21) the first term is zero and the last two terms sum to zero, the above equation can be further remarkably simplified as

$$\tilde{L}_{as}^{(\boldsymbol{\varphi}_r,\boldsymbol{\varphi}_r)} = \sum_{i=1}^{n_t}\left[\frac{N_{c,r,i}\tan^{-1}\kappa}{\nu_{r,i}\varsigma_{r,i}}\left(\boldsymbol{\varphi}_r^T\mathbf{B}_i\boldsymbol{\varphi}_r\right)^{-1}\boldsymbol{\Omega}_i\right] \tag{22}$$

As is seen from (22), each term corresponding to the $i$-th setup is dependent on the 'noise-to-environment' ratio $\nu_{r,i}=s_{\mu,r,i}/S_{f,r,i}$ . It is worth mentioning here that $S_{f,r,i}$ varies from one setup to another as its value depends on the adopted normalization of the mode shape. It can be argued that if local mode shape $\hat{\boldsymbol{\psi}}_{r,i}$ is scaled down (e.g., divided) by a factor then $S_{f,i}$ should be scaled up (e.g., multiplied) by the square of that same factor [38]. As is illustrated in the Appendix II, the 'noise-to-environment ratio' confined to the $i$-th setup can be approximately connected with the overall 'noise-to-environment ratio' $\nu_{r,all}$ corresponding to all measured dofs, which is given as follows:

$$\nu_{r,i} \approx \left(\boldsymbol{\varphi}_r^T\mathbf{B}_i\boldsymbol{\varphi}_r\right)^{-1}\nu_{r,all} \tag{23}$$

Substituting (23) into (22) leads to the approximated Hessian matrix of the Bayesian mode shape assembly algorithm:

$$L_{as}^{(\boldsymbol{\varphi}_r,\boldsymbol{\varphi}_r)} \approx \tilde{L}_{as}^{(\boldsymbol{\varphi}_r,\boldsymbol{\varphi}_r)} = \sum_{i=1}^{n_t}\left[\frac{N_{c,r,i}\tan^{-1}\kappa}{\left(\boldsymbol{\varphi}_r^T\mathbf{B}_i\boldsymbol{\varphi}_r\right)^{-1}\nu_{r,all}\,\varsigma_{r,i}}\left(\boldsymbol{\varphi}_r^T\mathbf{B}_i\boldsymbol{\varphi}_r\right)^{-1}\boldsymbol{\Omega}_i\right] = \sum_{i=1}^{n_t}\left[\frac{N_{c,r,i}\tan^{-1}\kappa}{\nu_{r,all}\,\varsigma_{r,i}}\boldsymbol{\Omega}_i\right] \tag{24}$$

In real applications with data processed in multiple setups, $\nu_{r,all}$ can be estimated using Eq.(23). Here we replace $\nu_{r,all}$ by using the averaged value estimated from different setups, i.e., $\bar{\nu}_{r,all}=\frac{1}{n_t}\sum_{i=1}^{n_t}\left(\boldsymbol{\varphi}_r^T\mathbf{B}_i\boldsymbol{\varphi}_r\right)\nu_{r,i}$ . Similarly, the damping ratio and 'normalized data length' corresponding to different setups are also replaced by the mean values $\bar{\varsigma}_r=\frac{1}{n_t}\sum_{i=1}^{n_t}\varsigma_{r,i}$ and $\bar{N}_{c,r}=\frac{1}{n_t}\sum_{i=1}^{n_t}N_{c,r,i}$ , then Eq. (24) can be further simplified as:

$$L_{as}^{(\boldsymbol{\varphi}_r,\boldsymbol{\varphi}_r)} \approx \tilde{L}_{as}^{(\boldsymbol{\varphi}_r,\boldsymbol{\varphi}_r)} = \frac{\bar{N}_{c,r}\tan^{-1}\kappa}{\bar{\varsigma}_r\bar{\nu}_{r,all}}\sum_{i=1}^{n_t}\boldsymbol{\Omega}_i \tag{25}$$

*3.3 Approximated posterior covariance matrix of the global mode shapes*

The posterior covariance matrix to the leading order can be obtained by taking the inverse of $\tilde{L}_{as}^{(\boldsymbol{\varphi}_r\boldsymbol{\varphi}_r)}$ shown in (25). $\tilde{L}_{as}^{(\boldsymbol{\varphi}_r\boldsymbol{\varphi}_r)}$ also has zero eigenvalues with eigenvectors parallel to the mode shape directions. This can be further illustrated by observing the first-derivative of the NLLF:

$$L_{as}^{(\boldsymbol{\varphi}_r)} = \sum_{i=1}^{n_t} \begin{bmatrix} -\left(\boldsymbol{\varphi}_r^T \mathbf{B}_i \boldsymbol{\varphi}_r\right)^{-2} \left(\boldsymbol{\varphi}_r^T \mathbf{A}_{r,i} \boldsymbol{\varphi}_r\right)\left(\mathbf{B}_i \boldsymbol{\varphi}_r\right) + \left(\boldsymbol{\varphi}_r^T \mathbf{B}_i \boldsymbol{\varphi}_r\right)^{-1} \left(\mathbf{A}_{r,i} \boldsymbol{\varphi}_r\right) \\ +\left(\boldsymbol{\varphi}_r^T \mathbf{B}_i \boldsymbol{\varphi}_r\right)^{-3/2} \left(\boldsymbol{\eta}_{r,i}^T \boldsymbol{\varphi}_r\right)\left(\mathbf{B}_i \boldsymbol{\varphi}_r\right) - \left(\boldsymbol{\varphi}_r^T \mathbf{B}_i \boldsymbol{\varphi}_r\right)^{-1/2} \boldsymbol{\eta}_{r,i} \end{bmatrix} \tag{26}$$

Substituting (16) and (19) into (26) results in

$$L_{as}^{(\boldsymbol{\varphi}_r)} \approx \tilde{L}_{as}^{(\boldsymbol{\varphi}_r)} = \sum_{i=1}^{n_t} \frac{N_{c,r,i} \tan^{-1}\kappa}{\nu_{r,i} \varsigma_{r,i}} \left[ -\left(\boldsymbol{\varphi}_r^T \mathbf{B}_i \boldsymbol{\varphi}_r\right)^{-2} \boldsymbol{\varphi}_r^T \boldsymbol{\Omega}_i \boldsymbol{\varphi}_r \left(\mathbf{B}_i \boldsymbol{\varphi}_r\right) + \left(\boldsymbol{\varphi}_r^T \mathbf{B}_i \boldsymbol{\varphi}_r\right)^{-1} \boldsymbol{\Omega}_i \boldsymbol{\varphi}_r \right] \tag{27}$$

The above equation can be rearranged as,

$$L_{as}^{(\boldsymbol{\varphi}_r)} \approx \tilde{L}_{as}^{(\boldsymbol{\varphi}_r)} = \frac{\bar{N}_c \tan^{-1}\kappa}{\bar{\varsigma}_r \bar{\nu}_{r,all}} \left[ \sum_{i=1}^{n_t} \boldsymbol{\Omega}_i \right] \boldsymbol{\varphi}_r \tag{28}$$

Due to the optimality of $\hat{\boldsymbol{\varphi}}_r$, $L_{as}^{(\boldsymbol{\varphi}_r)} = 0$, which suggests that

$$\frac{\bar{N}_{c,r} \tan^{-1}\kappa}{\bar{\varsigma}_r \bar{\nu}_{r,all}} \boldsymbol{\Omega} \hat{\boldsymbol{\varphi}}_r = 0 \times \hat{\boldsymbol{\varphi}}_r \tag{29}$$

where

$$\boldsymbol{\Omega} = \sum_{i=1}^{n_t} \boldsymbol{\Omega}_i = \sum_{i=1}^{n_t} \left[ \mathbf{B}_i - \mathbf{B}_i \hat{\boldsymbol{\varphi}}_r \hat{\boldsymbol{\varphi}}_r^T \mathbf{B}_i / (\hat{\boldsymbol{\varphi}}_r^T \mathbf{B}_i \hat{\boldsymbol{\varphi}}_r) \right] \tag{30}$$

The above equation demonstrates that the matrix $\boldsymbol{\Omega}$ has a zero eigenvalue with eigenvector $\boldsymbol{\varphi}_r$. Therefore, the irrelevant contributions from the singular terms (zero curvature) should be excluded when taking the inverse of $\tilde{L}_{as}^{(\boldsymbol{\varphi}_r\boldsymbol{\varphi}_r)}$.

Let $\{\tilde{\xi}_1,\tilde{\xi}_2,\cdots,\tilde{\xi}_{n_l}\}$ be the eigenvalues of $\mathbf{\Omega}$ estimated at the MPV of $\boldsymbol{\varphi}_r$ arranged in ascending order, while their corresponding eigenvectors are assumed to be $\{\tilde{\boldsymbol{\upsilon}}_1,\tilde{\boldsymbol{\upsilon}}_2,\cdots,\tilde{\boldsymbol{\upsilon}}_{n_l}\}$. As a result, the approximate covariance matrix $\tilde{\mathbf{C}}_{\boldsymbol{\varphi}_r}$ can be evaluated properly via its eigen-basis representation with the first smallest eigenvalue ignored,

$$\tilde{\mathbf{C}}_{\boldsymbol{\varphi}_r} \approx \frac{\bar{\varsigma}_r \bar{V}_{r,all}}{\bar{N}_{c,r}\tan^{-1}\kappa}\sum_{j=2}^{n_l}\tilde{\xi}_j^{-1}\tilde{\boldsymbol{\upsilon}}_j\tilde{\boldsymbol{\upsilon}}_j^T \tag{31}$$

Equation (31) provides insight related to the dependence of uncertainty on the various parameters. Specifically, the posterior uncertainty of the global mode shapes displays a decaying trend with the increase of bandwidth factor and time duration. However, the uncertainty is proportional to damping ratio and ‘signal-to-noise’ ratio.

### *3.4 Approximated overall uncertainty of the global mode shapes*

In [41], the idea of the Modal Assurance Criterion (MAC) in the deterministic case was extended to quantifying the uncertainty of the mode shape in a Bayesian context. Given the measured data, consider the MAC between the uncertain mode shape $\boldsymbol{\varphi}_r'$ and its optimal value $\hat{\boldsymbol{\varphi}}_r^T$. In a statistical sense, if the uncertainty in $\boldsymbol{\varphi}_r'$ is small, it will be close to $\hat{\boldsymbol{\varphi}}_r^T$, and the MAC will be close to unity. The MAC between $\boldsymbol{\varphi}_r'$ and $\hat{\boldsymbol{\varphi}}_r^T$ could be approximated by [41]

$$\tilde{M}_r = \frac{\hat{\boldsymbol{\varphi}}_r^T\boldsymbol{\varphi}_r'}{\left\|\hat{\boldsymbol{\varphi}}_r^T\right\|\left\|\boldsymbol{\varphi}_r'\right\|} = \left(1+\sum_{j=2}^{n_l}\tilde{\xi}_j^2 Z_j^2\right)^{-\frac{1}{2}} \tag{32}$$

where $Z_j$ denotes independent and identically distributed (i.i.d.) standard Gaussian random variables; $\tilde{\xi}_j$ be the eigenvalues of $\mathbf{\Omega}$ estimated at the MPV of $\boldsymbol{\varphi}_r$ arranged in ascending order.

According to [41], the expected MAC that quantifies the overall uncertainty of the global mode shape can be further approximated by the following equation:

$$E\left(\tilde{M}_r\right)=E\left(1+\sum_{j=2}^{n_l}\tilde{\xi}_j^2 Z_j^2\right)^{-\frac{1}{2}}\approx\left(1+\tilde{\delta}_{\varphi_r}^2\right)^{-\frac{1}{2}} \tag{33}$$

where $\tilde{\delta}_{\varphi_r}^2$ is the sum of principle variances of $\tilde{\mathbf{C}}_{\varphi_r}$ (i.e., the trace of covariance matrix), which can be calculated by employing the approximated covariance matrix (i.e., Eq.(31)):

$$\tilde{\delta}_{\varphi_r}^2=tr\left(\tilde{\mathbf{C}}_{\varphi_r}\right)=\frac{\overline{\varsigma}_r\overline{V}_{r,all}}{\overline{N}_{c,r}\tan^{-1}\kappa}tr\left(\sum_{j=2}^{n_l}\tilde{\xi}_j^{-1}\tilde{\mathbf{v}}_j\tilde{\mathbf{v}}_j^T\right) \tag{34}$$

For the purpose of comparison, the expected MAC for the 'exact' covariance matrix of the global mode shapes computed by taking the inverse of the original Hessian matrix without resorting to the approximation strategy (i.e., (11)) are also presented here

$$E\left(M_r\right)=\left(1+\delta_{\varphi_r}^2\right)^{-\frac{1}{2}} \tag{35}$$

where

$$\delta_{\varphi_r}^2=tr\left(\mathbf{C}_{\varphi_r}\right)=tr\left(\sum_{j=2}^{n_l}\xi_j'^{-1}\mathbf{v}_j'\mathbf{v}_j'^T\right) \tag{36}$$

## 4 Numerical Study

A 15-story shear building with separated modes is adopted as a numerical example to illustrate the accuracy of the proposed theory. Classical Rayleigh damping with the damping ratios for the first two modes set to be 1% is assumed. The stiffness and mass for each dof is assumed to be $250000kN/m$ and $100kg$, respectively. The structure is excited by ambient excitation modelled using Gaussian white noise with auto-spectral intensity $1.5m^2s^{-3}$. To verify the efficiency of the explicit approximation of Bayesian mode shape assembly method, the 15 dofs are assumed to be covered by four setups, and the setup information is shown in Table 1. For each setup, the modal properties as well as their uncertainties are identified using fast Bayesian FFT approach [31]. The identified spectral variables including the most probable values ($\hat{\theta}$), the standard deviation ($\sigma$) and the coefficients of variances ($\sigma/\hat{\theta}$) are presented in Table 2. The partial mode shapes corresponding to different setups are to be assembled using the algorithm introduced in Section 2 and 3. The 'exact' values of the posterior variances of the global mode shapes are computed by taking the inverse of $L_{as}^{(\varphi_r,\varphi_r)}$ (i.e. Eq. (11)) neglecting the irrelevant contributions from the singular terms (zero curvature). For the special case with $\kappa$=6 and $T$=1000s , the optimal values and two times the posterior standard deviation of the first four mode shape components are illustrated in Fig. 3.

Table 1: Setup information for the shear building

| Setup | Measured dofs |
|---|---|
| 1 | 1, 2, 3, 4, 5 |
| 2 | 4, 5, 6, 7, 8 |
| 3 | 8,9,10,11,12 |
| 4 | 11,12,13,14,15 |

Table 2. Identified spectrum variables of the numerical study

| Mode | $\kappa$ | Variable | Values | | |
|---|---|---|---|---|---|
| | | | $\hat{\theta}$ | $\sigma$ | $\sigma/\hat{\theta}$ (%) |
| 1 | 6 | $f_1$ | 0.8081 | 0.0035 | 0.44 |
| | | $\varsigma_1$ | 0.0104 | 0.0027 | 25.63 |
| | | $S_f$ | 0.0154 | 0.0038 | 24.63 |
| | | $s_\mu$ | 7.0630 | 0.0233 | 0.33 |
| 2 | 6 | $f_2$ | 2.4114 | 0.0032 | 0.13 |
| | | $\varsigma_2$ | 0.0122 | 0.0045 | 36.76 |
| | | $S_f$ | 0.1012 | 0.0358 | 35.42 |
| | | $s_\mu$ | 7.2739 | 0.1422 | 1.95 |
| 3 | 6 | $f_3$ | 3.9919 | 0.0046 | 0.11 |

| | | | | | |
|---|---|---|---|---|---|
| | | $\varsigma_3$ | 0.0132 | 0.0035 | 26.68 |
| | | $S_f$ | 0.1018 | 0.0257 | 5.21 |
| | | $s_{\mu}$ | 7.4578 | 0.0374 | 0.50 |
| 4 | 6 | $f_4$ | 5.5361 | 0.0086 | 0.16 |
| | | $\varsigma_4$ | 0.0201 | 0.0018 | 8.80 |
| | | $S_f$ | 0.0844 | 0.0061 | 7.22 |
| | | $s_{\mu}$ | 7.4425 | 0.0115 | 0.15 |

Note: here $\hat{\theta}$ denotes the most probable values; $\sigma$ denotes standard deviation; $\sigma/\hat{\theta}$ denotes coefficients of variances.

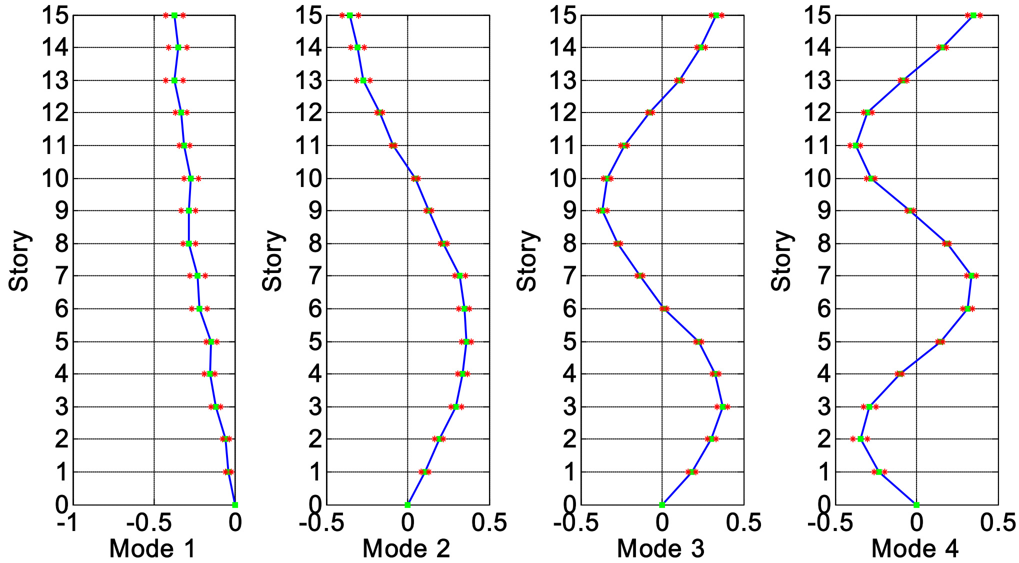


Fig. 3: The optimal values (square) and two times standard deviation (asterisk) of the assembled global mode shapes (numerical study)

To verify the accuracy of the approximate formula of the posterior uncertainty of the global mode shapes, the expected MAC obtained from the 'exact' numerical algorithm calculated from (13) and the 'approximate' strategy calculated using (31) will be compared with each other. The effects of the bandwidth and noise level on the posterior uncertainty of the global mode shapes will also be observed here in detail. Assume that the bandwidth factor varies from 2 to 12 at an increment of 1 while the data duration is fixed to be 900 seconds. The exact posterior overall uncertainty ( $1\text{-}E\left(M_r\right)$ ) and approximate overall uncertainty ($1\text{-}E\left(\tilde{M}_r\right)$) with different bandwidth factor are compared in Fig. 4. To examine the effect of noise level, a number of values of $1\text{-}E\left(M_r\right)$ and $1\text{-}E\left(\tilde{M}_r\right)$ are obtained using the responses subject to different noise level, with its PSD ranging from 0 to $1m^2s^{-3}$ at an increment of $0.1m^2s^{-3}$ while the bandwidth used for each mode is fixed at $\kappa=6$. The results versus noise level are shown in Fig. 5. In Fig.4 and 5, the 'exact' values of posterior c.o.v. are denoted by markers, while the 'approximate' values of posterior c.o.v. are represented by solid lines.

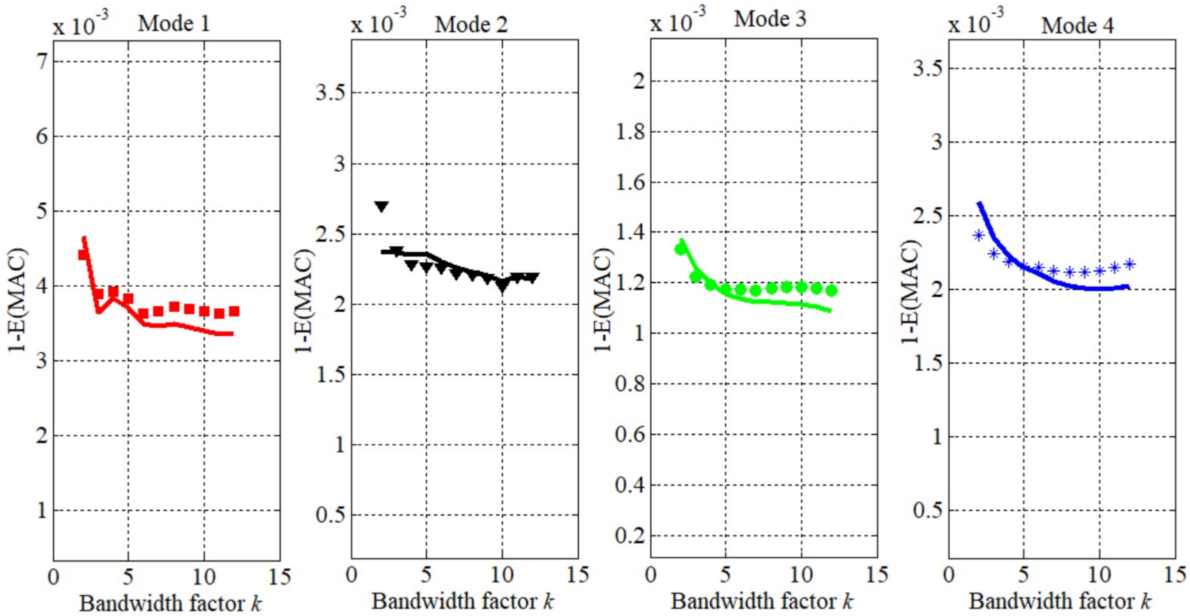


Fig. 4: Comparison of the overall uncertainty of the global mode shapes with 'exact' method denoted by markers and 'approximate' method denoted by solid lines versus bandwidth factor (numerical study)

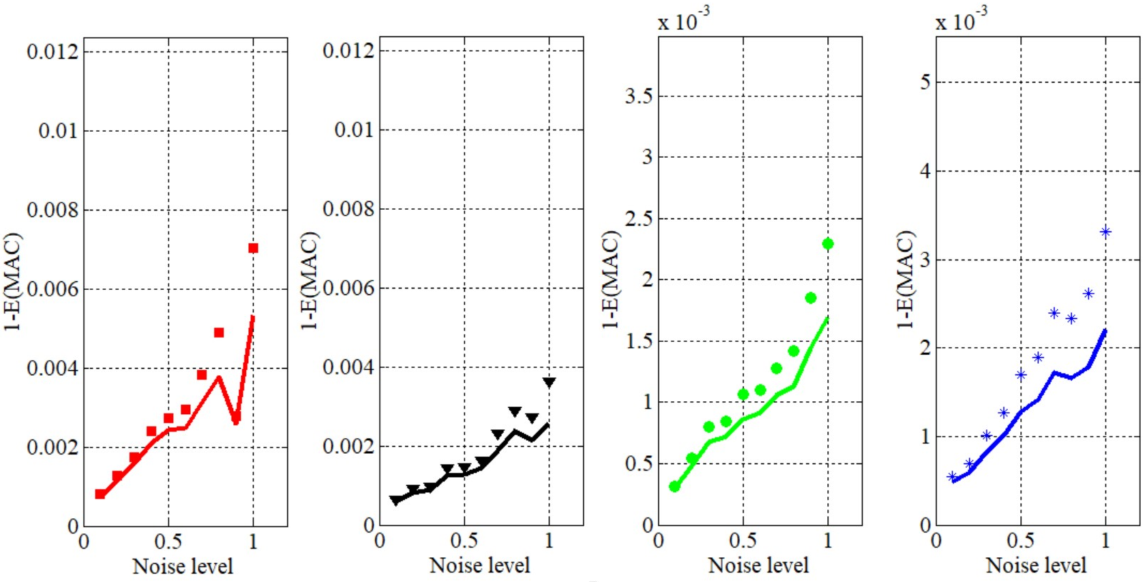


Fig. 5: Comparison of the overall uncertainty of the global mode shapes with 'exact' method denoted by markers and 'approximate' method denoted by solid lines versus noise level (numerical study).

From Fig. 4 and 5, one can figure out that, although there are discrepancies between the 'exact' values and 'approximate' values, the order of the uncertainty of the global mode shapes estimated using two different kinds of approaches are in the same level, indicating that the proposed approximate formula approaches the posterior uncertainty of the assembled overall mode shapes with satisfactory accuracy. Furthermore, the posterior uncertainty of the global mode shapes displays a slight decaying trend with the increase of bandwidth factor, while an increasing trend is revealed with the increase of noise level. This is consistent with previous results [39] which state that the uncertainty reduces with more available information but increases with the higher 'noise-to-signal' ratio.

## 5 Experimental Study

We next consider a real application of the Metsovo bridge located in Greece . The bridge crosses the deep ravine of Metsovitikos river with 150m over the riverbed. The bridge is a 4-span continues concrete highway bridge. The total length of the bridge is 537 m with a span layout of (44.78+117.87+235+140) m. The bridge has 3 piers: M1 (45m) supporting the box beam superstructure through pot bearings is movable in both horizontal directions, while M2 (110m) and M3 (35m) piers connect monolithically to the structure. The sideview of the bridge is shown in Fig. 6.

Fig. 6: The sideview of the Metsovo bridge [45]

Fig. 7: Experimental setups of ambient vibration test for the Metsovo bridge [45]

Ambient vibration test was conducted to measure the responses of the Metsovo bridge mainly due to road traffic, which ranged from light vehicles to heavy trucks, and environmental excitation such as wind loading by using a wireless measurement system. The wireless measurement system mainly consisted of 5 triaxial and 3 uniaxial accelerometers paired with a 24-bit data recording system, a GPS module for synchronization between sensors, and a battery pack. The wireless measurement system is connected with a laptop that can set sampling rate, recording duration, repeater recordings, etc. and visualize the measurements. The instrumentation is shown in Fig. 7.

The entire length of the deck was covered by 13 sensor configurations which produced 159 sensor locations. Each configuration recorded for 20 minutes at a sampling rate of 100 Hz. A typical example of indicative sensor configuration is illustrated in Fig. 8. The points stressed by green face correspond to reference sensors including one triaxial (i.e., station 11 in Fig.8) and three uniaxial sensors (i.e., station 39 in vertical direction and station 40 and 42 in horizontal direction), which were obtained by minimizing the information entropy using an optimal sensor location theory [42-44] to provide the highest information content for identifying the modal parameters of the structure. The points in blue color denote the moving sensors of the specific sensor configuration. The three numbers above each point in Fig. 8 correspond to the three measured dofs in the three directions measured by the triaxial sensors. The measurement stations arrangement for each setup is shown in Table 3. More details on the ambient vibration test of the Metsovo bridge are referred to [45,46].

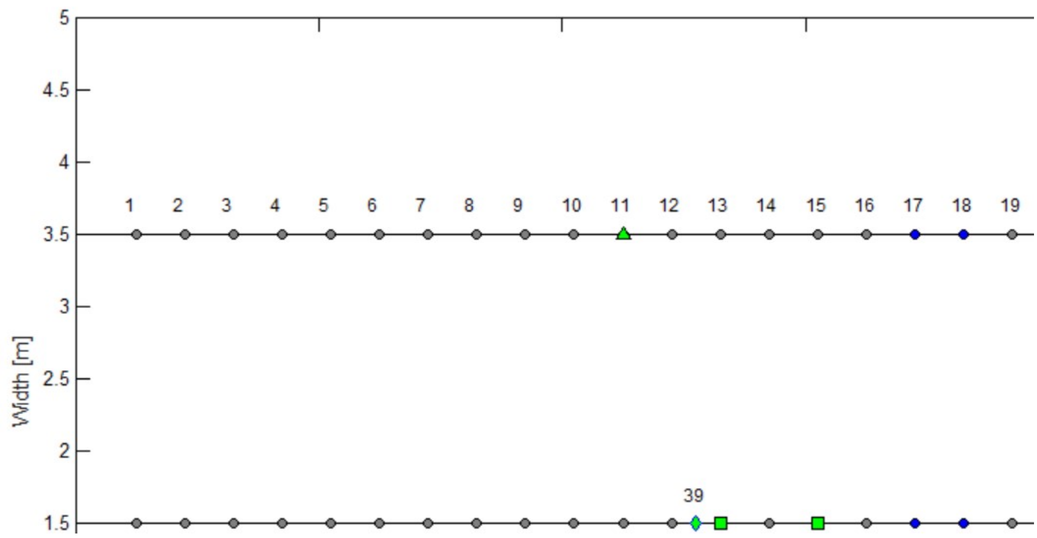


Fig. 8: Sensor configuration for the ambient vibration test of the Metsovo bridge

Table 3. Measurement setups of the Metsovo Bridge

| Setup | Measurement stations | Reference stations |
|---|---|---|
| 1 | 13;40;14;41 | 11(triaxial sensor); 39 (uniaxial sensor); 40(uniaxial sensor); 42(uniaxial sensor) |
| 2 | 15;42;16;43 | |
| 3 | 17;44; 18;45 | |
| 4 | 19;46; 20;47 | |
| 5 | 21;48; 22;49 | |
| 6 | 23;50;24;51 | |
| 7 | 25;52; 26;53 | |
| 8 | 1;27; 2;28 | |
| 9 | 3;29;4;30 | |
| 10 | 5;31;6;32 | |
| 11 | 7;33;8;34 | |
| 12 | 9;35;10;36 | |
| 13 | 11;37;12;38 | |

Ambient acceleration data of each configuration are processed to identify the modal properties including the modal frequencies, damping ratios, PSD of the modal excitation, PSD of the prediction error as well as the local mode shapes. The raw PSD computed using the acceleration of the transverse and vertical measurements are shown in Fig. 9(a) and 9(b), respectively. The ambient modal identification uses Bayesian operational modal analysis approach based on the FFT in specific frequency bands of interest. It is worth mentioning here that the acceleration data acquired by sensors in the vertical and transverse directions are processed separately to make sure that the separated modes assumption is satisfied.

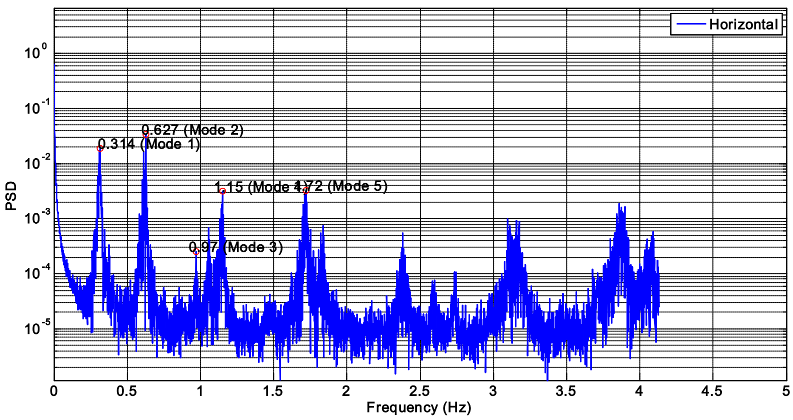


(a) Transverse direction

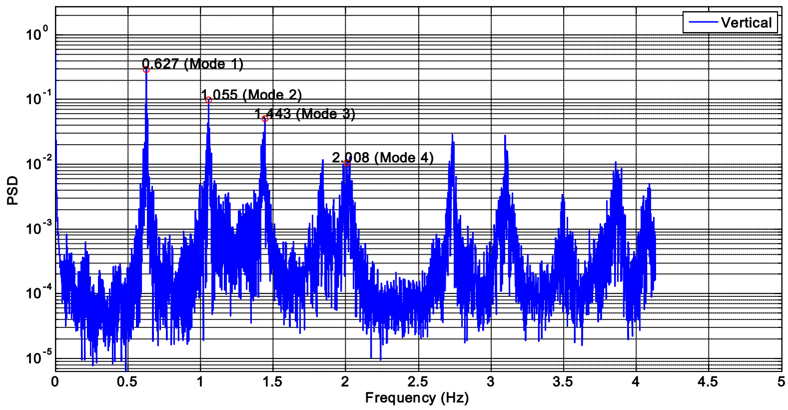


(b) Vertical direction

Fig. 9: PSD of the accelerations in the transverse direction and vertical direction

Table 4 presents the frequencies and damping ratios for the first five transverse bending modes and the first four vertical bending modes when the measurements of the second sensor configuration was employed. The bandwidth factor and time duration are fixed at $\kappa = 6$ and $T = 1200s$. Due to the fact that the modal properties were identified from each of the 13 sensor configurations separately, their values vary from one configuration to the other. The variation of the natural frequency is small, while the fluctuation in the remaining parameters is more significant.

Table 4. Identified spectrum variables of the Metsovo Bridge with $\kappa = 6$

| Modes | | Natural Frequency | | | Damping Ratio | | |
|---|---|---|---|---|---|---|---|
| | | $\hat{\theta}$ | $\sigma$ | $\sigma/\hat{\theta}$ (%) | $\hat{\theta}$ | $\sigma$ | $\sigma/\hat{\theta}$ (%) |
| Transverse Modes | 1 | 0.3106 | 0.0013 | 0.41 | 0.0219 | 0.0057 | 26.00 |
| | 2 | 0.6200 | 0.0011 | 0.18 | 0.0118 | 0.0022 | 18.66 |
| | 3 | 0.9693 | 0.0018 | 0.18 | 0.0118 | 0.0029 | 24.44 |
| | 4 | 1.1431 | 0.0012 | 0.11 | 0.0082 | 0.0012 | 15.02 |
| | 5 | 1.7169 | 0.0016 | 0.09 | 0.0092 | 0.0011 | 11.95 |
| Vertical Modes | 1 | 0.6267 | 0.0008 | 0.13 | 0.0069 | 0.0014 | 20.55 |
| | 2 | 1.0591 | 0.0018 | 0.17 | 0.0184 | 0.0019 | 10.13 |
| | 3 | 1.4233 | 0.0017 | 0.12 | 0.0119 | 0.0014 | 11.34 |
| | 4 | 1.9632 | 0.0042 | 0.22 | 0.0330 | 0.0035 | 10.56 |

Note: $\hat{\theta}$ denotes most probable values; $\sigma$ denotes standard deviation; $\sigma/\hat{\theta}$ denotes coefficients of variances.

In this vibration test, one triaxial and three uniaxial sensors (one vertical and two horizontal) remained in the same position throughout the measurements as reference dofs provide common measurement points amongst different configurations so as to enable the assembling of the mode shapes from partial mode shape components. The mode shape assembly methodology introduced in Section 2 is adopted here to combine the mode shape components of each configuration to produce the full mode shapes at all 159 sensor locations covered by the 13 configurations. The first five transverse bending modes as well as the first four vertical bending modes were illustrated in Fig. 10 and Fig. 11, respectively. The 5th vertical local mode shapes were very poorly identified and thus they were excluded from the set. From comparisons between the identified mode shapes (left column) and those calculated using FEM (right column) shown in Fig 10 and 11, one can clearly figure out that the Bayesian mode shape assembly algorithm has satisfactory performance.

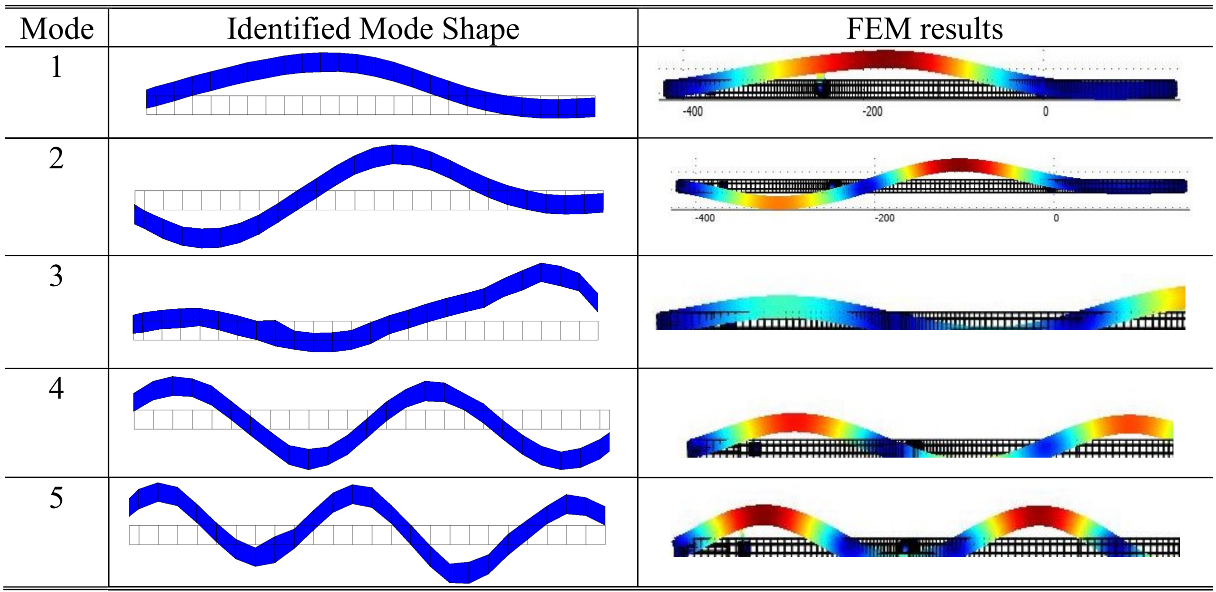


Fig. 10: Comparison between the experimentally identified (left column) and nominal FE model predicted (right column) transverse bending mode shapes of the Metsovo bridge

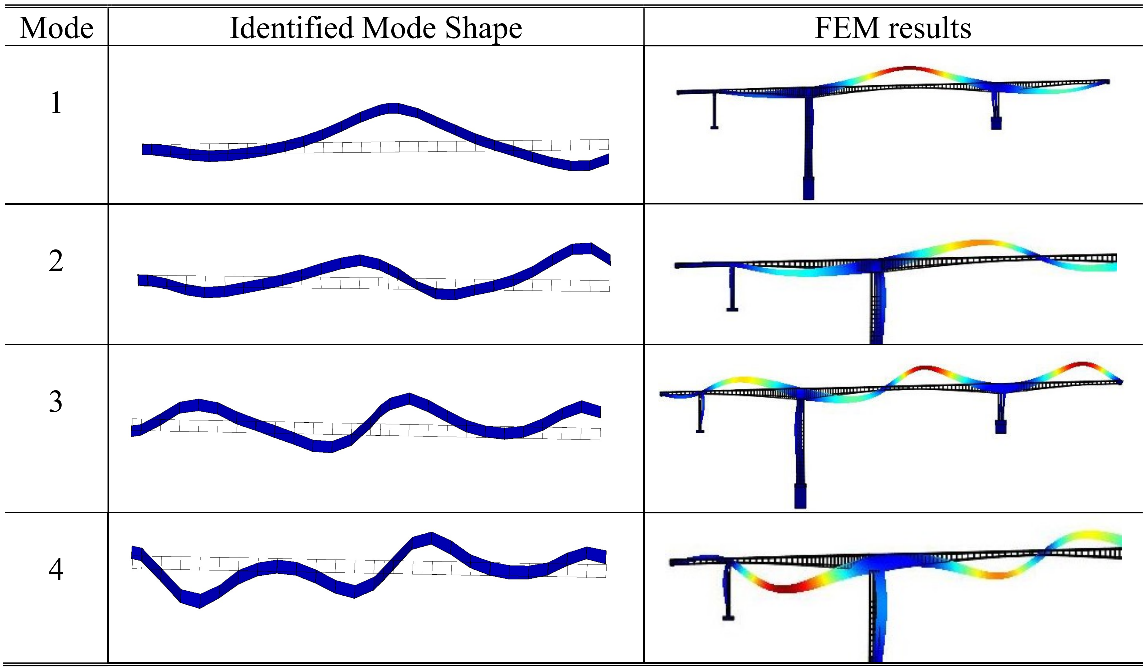


Fig. 11: Comparison between the experimentally identified (left column) and nominal FE model predicted (right column) vertial bending mode shapes of the Metsovo bridge

The effects of the bandwidth factor and data length on the uncertainty behavior of modal properties were investigated in detail: (i) The bandwidth factor varies from 1 to 14 at an increment of 1 with the time duration being fixed at 1200 seconds. The values of $1\text{-}E\left(MAC\right)$ of the assembled global mode shapes are shown in Fig. 12. (ii) The data duration ranges from 400 to 1200 seconds at an increment of 100 seconds with the bandwidth and the number of data sets being fixed at $\kappa = 8$. The variation of the overall uncertainty of the assembled global mode shapes are compared in Fig.13. The 'exact' values of the posterior variances are computed by taking the exact inverse of $L_{as}^{(\varphi_r,\varphi_r)}$ using Eq. (11), while the 'approximate' posterior covariances can be calculated using Eq. (31). The results of the 'exact' and 'approximate' values of $1\text{-}E\left(MAC\right)$ are denoted by discrete marked points and continuous lines, respectively. The first few modes of the 'exact' values are denoted by square, triangles, circle, asterisk and diamond, respectively. From these figures, one can draw the following conclusions:

- The closed-form formulas generally give a satisfactory approximation of the exact values for most of the cases. In some cases, however, the 'approximated' values of $1\text{-}E(MAC)$ deviate from the 'exact' values with quite significant error as the assumption for large $N_c$ is violated when the bandwidth factor is small.
- Ideally, according to the approximate formulas, the results for each mode should form a smoothed line when bandwidth factor and time duration varies. However, the observed deviation from a smoothed line is mainly due to the fluctuation in the MPV of modal parameters when different data durations are used. The posterior uncertainty of the global mode shapes displays a decaying trend with the increase of bandwidth factor and time duration. This can be expected from (31) that the uncertainty is inverse proportional to the bandwidth factor $\kappa$ and the time duration $T_d$.
- The posterior uncertainty converges quickly with the increase of time duration and bandwidth factor. The phenomenon indicates that when the modal 'signal-to-noise' ratio is sufficiently high, increasing the time duration and frequency band does not significantly improve the mode shape assembly quality.

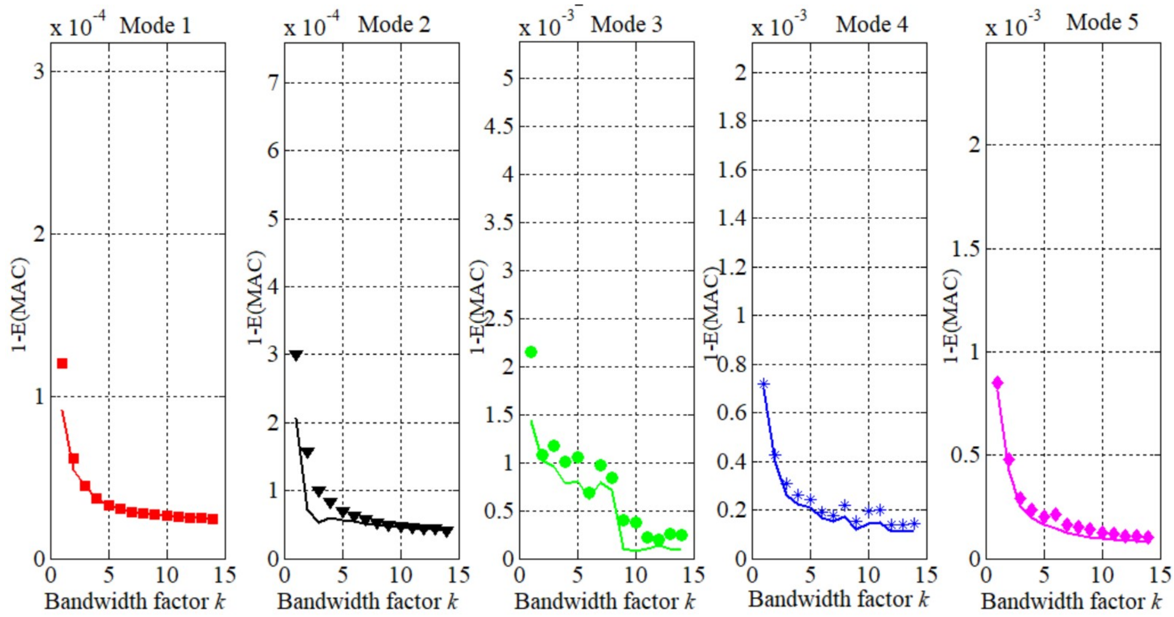


(a) First five transverse bending modes

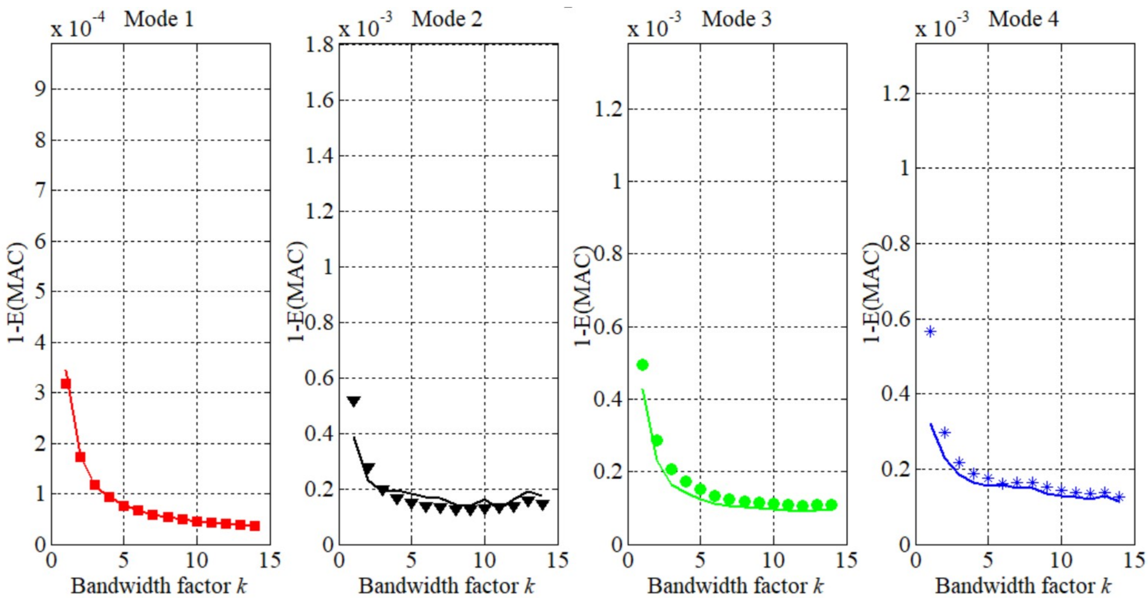


(b) First four vertical bending modes

Fig.12: Posterior overall uncertainty of the assembled global mode shapes versus bandwidth factor (experimental study): the ‘exact’ values are denoted by markers and the ‘approximate’ values are represented by solid lines.

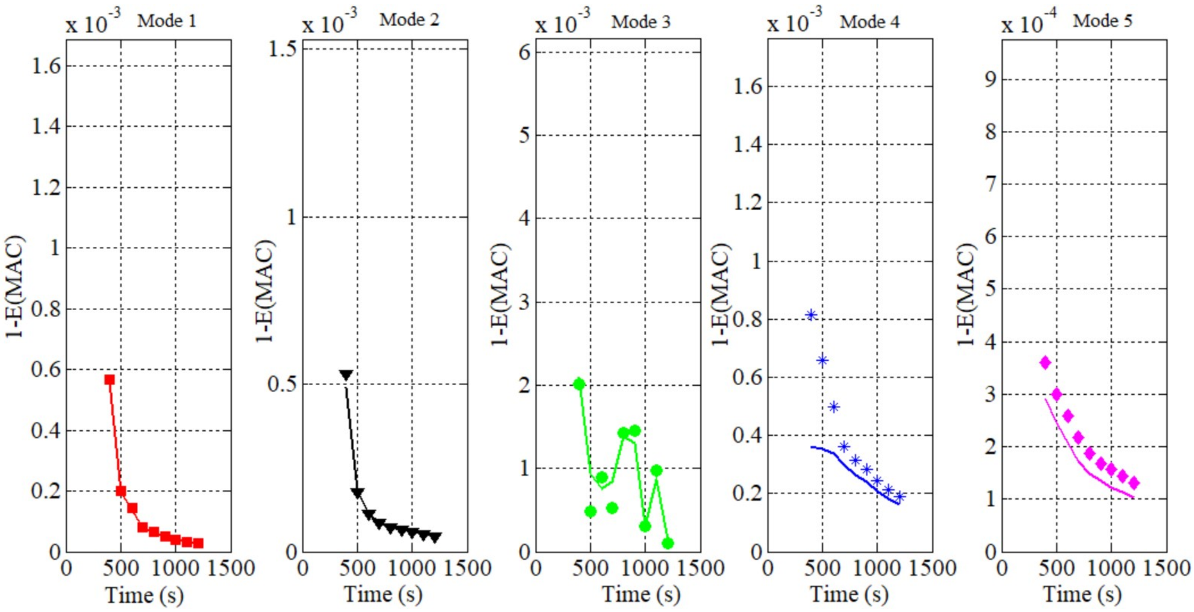


(a) First five transverse bending modes

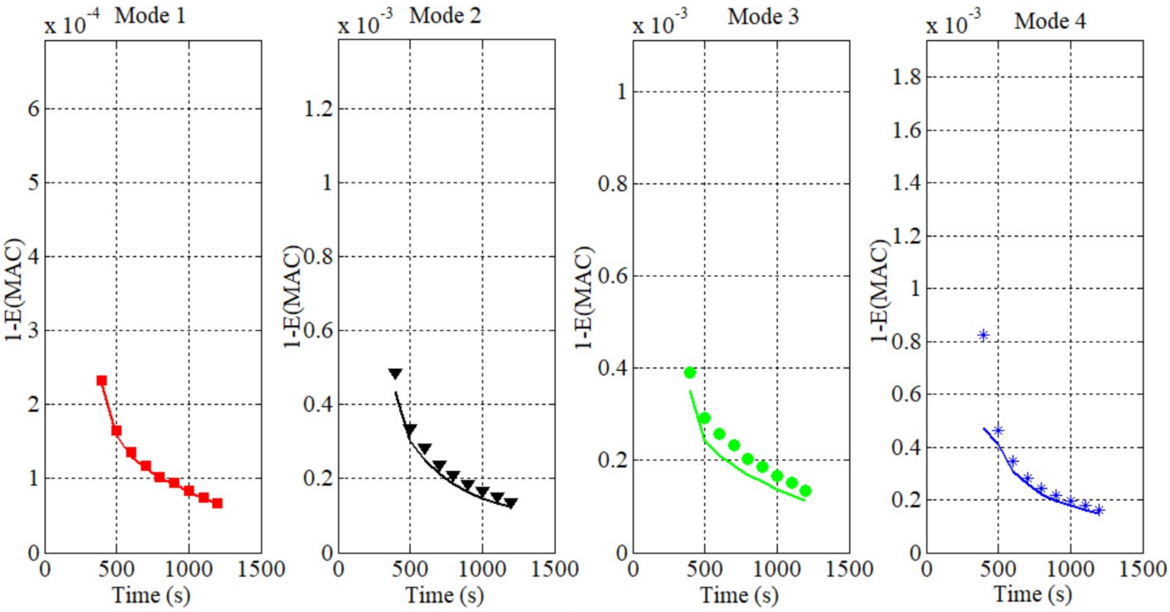


(b) First four vertical bending modes

Fig. 13: Posterior overall uncertainty of the assembled global mode shapes versus time duration (experimental study): the ‘exact’ values are denoted by markers and the ‘approximate’ values are represented by solid lines.

## 6 Concluding Remarks

The mode shape assembly, assembling identified local mode shapes from different setups to form global mode shapes, is of critical importance as it allows exploiting the computational autonomous capabilities of different clusters and avoid simultaneous measurements of data of all setups when the sensors are limited. Inspired by the uncertainty law of ambient modal analysis [38,39], this paper provided a deeper understanding of the intrinsic uncertainty propagation behavior of global mode shapes obtained when using the Bayesian mode shape assembly approach. Explicit approximate formulas for the posterior covariance matrix in terms of spectrum modal parameters (e.g., natural frequency, damping ratio, PSD of modal excitation and prediction error) and data information parameters (e.g., the spectral bandwidth factor and the data duration of measurements) are derived analytically given that the damping ratio for the structure is assumed to be small, the 'noise-to-signal ratio' is small, and the data duration is long. A numerical example and a real application of the Metsovo bridge equipped with wireless sensors were employed to validate the theories. Satisfactory agreements are found between the ‘approximation’ and the ‘exact’ values of the posterior uncertainties, which indicates that the closed-from approximation formulas are able to represent the trends in uncertainty variations. Thus the approximate formulas can be used to provide new insights into how the posterior uncertainties in the local mode shapes identified using the fast Bayesian approach propagate into the assembled global mode shapes.

This approximate analysis in this study also provides insights on the main contribution of different parameters to the uncertainty of mode shape assembly. As is seen from Eq. (31), the posterior covariance of global mode shapes depends on the following dimensionless scales: the damping ratio, which is a property of the tested structure; the 'bandwidth factor' (i.e., the amount of information actually utilized); the 'noise-to-environment' ratio which is related to a modal noise-to-signal ratio; the 'normalized data length' which represent the amount of information available in the data; the selection matrix denoting the sensor configuration in ambient vibration test. In particular, the posterior covariance matrix of the global mode shapes is inversely proportional to 'normalized data length' and the 'bandwidth factor', and propositional to 'noise-to-environment' ratio and damping ratio. This indicates that the accuracy of global mode shapes can be improved by using better quality equipment, longer measurements and increasing the frequency bandwidth properly.

This study highlights the strengths of the Bayesian approach applied in modal analysis, allowing the quantification and propagation of uncertainties with respect to different parameters. The results have implications on the extent to which one can reduce uncertainty and planning for ambient vibration tests when using the technique, as is illustrated in [38,39]. Furthermore, it is worth mentioning here that one can extend the framework by minimizing Eq.(31) to address the optimal sensor placement problem when multiple setups are considered in real vibration test. The optimal sensor placement for global mode shape estimation is left for future endeavor.

**Acknowledgments**

This first author was supported by the Marie Sklodowska-Curie individual Fellowships of the EU under Contract 741284 when visiting the University of Nottingham. Prof. Lambros Katafygiotis highly appreciates the funding provided by the Hong Kong Research Grants Council under grants 16234816 and 16212918.

## Appendix I: New derivation of the Hessian matrix of Bayesian mode shape assembly

The NLLF of (4) can be expanded as

$$\begin{aligned}
L_{as} &= \frac{1}{2}\sum_{i=1}^{n_t}\left(\mathbf{L}_i\boldsymbol{\varphi}_r / \|\mathbf{L}_i\boldsymbol{\varphi}_r\| - \hat{\boldsymbol{\psi}}_{r,i}\right)^T \mathbf{C}_{\boldsymbol{\psi}_{r,i}}^{-1}\left(\mathbf{L}_i\boldsymbol{\varphi}_r / \|\mathbf{L}_i\boldsymbol{\varphi}_r\| - \hat{\boldsymbol{\psi}}_{r,i}\right) \\
&= \frac{1}{2}\sum_{i=1}^{n_t}\left[\boldsymbol{\varphi}_r^T\mathbf{L}_i^T\mathbf{C}_{\boldsymbol{\psi}_{r,i}}^{-1}\mathbf{L}_i\boldsymbol{\varphi}_r \Big/ \|\mathbf{L}_i\boldsymbol{\varphi}_r\|^2 - 2\hat{\boldsymbol{\psi}}_{r,i}^T\mathbf{C}_{\boldsymbol{\psi}_{r,i}}^{-1}\mathbf{L}_i\boldsymbol{\varphi}_r \Big/ \|\mathbf{L}_i\boldsymbol{\varphi}_r\| + \hat{\boldsymbol{\psi}}_{r,i}^T\mathbf{C}_{\boldsymbol{\psi}_{r,i}}^{-1}\mathbf{L}_i\hat{\boldsymbol{\psi}}_{r,i}\right] \\
&= \frac{1}{2}\sum_{i=1}^{n_t}\left[\left(\boldsymbol{\varphi}_r^T\mathbf{B}_i\boldsymbol{\varphi}_r\right)^{-1}\left(\boldsymbol{\varphi}_r^T\mathbf{A}_{r,i}\boldsymbol{\varphi}_r\right) - 2\left(\boldsymbol{\varphi}_r^T\mathbf{B}_i\boldsymbol{\varphi}_r\right)^{-\frac{1}{2}}\left(\boldsymbol{\eta}_{r,i}^T\boldsymbol{\varphi}_r\right) + \left(\hat{\boldsymbol{\psi}}_{r,i}^T\mathbf{C}_{\boldsymbol{\psi}_{r,i}}^{-1}\hat{\boldsymbol{\psi}}_{r,i}\right)\right]
\end{aligned} \tag{A1}$$

where

$$\mathbf{A}_{r,i} = \mathbf{L}_i^T\mathbf{C}_{\boldsymbol{\psi}_{r,i}}^{-1}\mathbf{L}_i \tag{A2a}$$

$$\mathbf{B}_i = \mathbf{L}_i^T\mathbf{L}_i \tag{A2b}$$

$$\boldsymbol{\eta}_{r,i}^T = \hat{\boldsymbol{\psi}}_{r,i}^T\mathbf{C}_{\boldsymbol{\psi}_{r,i}}^{-1}\mathbf{L}_i \tag{A2c}$$

The derivative of $L_{as}$ with respect to $\boldsymbol{\varphi}_r$ denoted by $L_{as}^{(\boldsymbol{\varphi}_r)}$ is given by

$$\begin{aligned}
L_{as}^{(\boldsymbol{\varphi}_r)} &= \frac{1}{2}\sum_{i=1}^{n_t}\left\{\begin{array}{l}\left[\left(\boldsymbol{\varphi}_r^T\mathbf{B}_i\boldsymbol{\varphi}_r\right)^{-1}\right]^{(\boldsymbol{\varphi}_r)}\left(\boldsymbol{\varphi}_r^T\mathbf{A}_{r,i}\boldsymbol{\varphi}_r\right) + \left(\boldsymbol{\varphi}_r^T\mathbf{B}_i\boldsymbol{\varphi}_r\right)^{-1}\left(\boldsymbol{\varphi}_r^T\mathbf{A}_{r,i}\boldsymbol{\varphi}_r\right)^{(\boldsymbol{\varphi}_r)} \\ -2\left(\left[\left(\boldsymbol{\varphi}_r^T\mathbf{B}_i\boldsymbol{\varphi}_r\right)^{-1/2}\right]^{(\boldsymbol{\varphi}_r)}\left(\boldsymbol{\eta}_{r,i}^T\boldsymbol{\varphi}_r\right) + \left(\boldsymbol{\eta}_{r,i}^T\boldsymbol{\varphi}_r\right)^{(\boldsymbol{\varphi}_r)}\left(\boldsymbol{\varphi}_r^T\mathbf{B}_i\boldsymbol{\varphi}_r\right)^{-1/2}\right)\end{array}\right\} \\
&= \sum_{i=1}^{n_t}\left[\begin{array}{l}-\left(\boldsymbol{\varphi}_r^T\mathbf{B}_i\boldsymbol{\varphi}_r\right)^{-2}\left(\boldsymbol{\varphi}_r^T\mathbf{A}_{r,i}\boldsymbol{\varphi}_r\right)\left(\mathbf{B}_i\boldsymbol{\varphi}_r\right) + \left(\boldsymbol{\varphi}_r^T\mathbf{B}_i\boldsymbol{\varphi}_r\right)^{-1}\left(\mathbf{A}_{r,i}\boldsymbol{\varphi}_r\right) \\ +\left(\boldsymbol{\varphi}_r^T\mathbf{B}_i\boldsymbol{\varphi}_r\right)^{-3/2}\left(\boldsymbol{\eta}_{r,i}^T\boldsymbol{\varphi}_r\right)\left(\mathbf{B}_i\boldsymbol{\varphi}_r\right) - \left(\boldsymbol{\varphi}_r^T\mathbf{B}_i\boldsymbol{\varphi}_r\right)^{-1/2}\boldsymbol{\eta}_{r,i}\end{array}\right]
\end{aligned} \tag{A3}$$

By differentiating (A3), one can obtain the derivative of $L_{as}^{(\boldsymbol{\varphi}_r)}$ with respect to $\boldsymbol{\varphi}_r$,

$$
\begin{aligned}
L_{as}^{(\boldsymbol{\varphi}_r\boldsymbol{\varphi}_r)} &= \sum_{i=1}^{n_t}\begin{bmatrix} -\left(\boldsymbol{\varphi}_r^T\mathbf{B}_i\boldsymbol{\varphi}_r\right)^{-2}\left(\boldsymbol{\varphi}_r^T\mathbf{A}_{r,i}\boldsymbol{\varphi}_r\right)\left(\mathbf{B}_i\boldsymbol{\varphi}_r\right)+\left(\boldsymbol{\varphi}_r^T\mathbf{B}_i\boldsymbol{\varphi}_r\right)^{-1}\left(\mathbf{A}_{r,i}\boldsymbol{\varphi}_r\right) \\ +\left(\boldsymbol{\varphi}_r^T\mathbf{B}_i\boldsymbol{\varphi}_r\right)^{-3/2}\left(\boldsymbol{\eta}_{r,i}^T\boldsymbol{\varphi}_r\right)\left(\mathbf{B}_i\boldsymbol{\varphi}_r\right)-\left(\boldsymbol{\varphi}_r^T\mathbf{B}_i\boldsymbol{\varphi}_r\right)^{-1/2}\boldsymbol{\eta}_{r,i} \end{bmatrix}^{(\boldsymbol{\varphi}_r)} \\
&= \sum_{i=1}^{n_t}\begin{bmatrix} -\left[\left(\boldsymbol{\varphi}_r^T\mathbf{B}_i\boldsymbol{\varphi}_r\right)^{-2}\left(\boldsymbol{\varphi}_r^T\mathbf{A}_{r,i}\boldsymbol{\varphi}_r\right)\left(\mathbf{B}_i\boldsymbol{\varphi}_r\right)\right]^{(\boldsymbol{\varphi}_r)}+\left[\left(\boldsymbol{\varphi}_r^T\mathbf{B}_i\boldsymbol{\varphi}_r\right)^{-1}\left(\mathbf{A}_{r,i}\boldsymbol{\varphi}_r\right)\right]^{(\boldsymbol{\varphi}_r)} \\ +\left[\left(\boldsymbol{\varphi}_r^T\mathbf{B}_i\boldsymbol{\varphi}_r\right)^{-3/2}\left(\boldsymbol{\eta}_{r,i}^T\boldsymbol{\varphi}_r\right)\left(\mathbf{B}_i\boldsymbol{\varphi}_r\right)\right]^{(\boldsymbol{\varphi}_r)}-\left[\left(\boldsymbol{\varphi}_r^T\mathbf{B}_i\boldsymbol{\varphi}_r\right)^{-1/2}\boldsymbol{\eta}_{r,i}\right]^{(\boldsymbol{\varphi}_r)} \end{bmatrix}
\end{aligned}
\tag{A4}
$$

Four different terms involved in (A4) can be further arranged as

$$
\begin{aligned}
&\left[\left(\boldsymbol{\varphi}_r^T\mathbf{B}_i\boldsymbol{\varphi}_r\right)^{-2}\left(\boldsymbol{\varphi}_r^T\mathbf{A}_{r,i}\boldsymbol{\varphi}_r\right)\left(\mathbf{B}_i\boldsymbol{\varphi}_r\right)\right]^{(\boldsymbol{\varphi}_r)} \\
&=\left(\boldsymbol{\varphi}_r^T\mathbf{B}_i\boldsymbol{\varphi}_r\right)^{-2}\left[\left(\boldsymbol{\varphi}_r^T\mathbf{A}_{r,i}\boldsymbol{\varphi}_r\right)\left(\mathbf{B}_i\boldsymbol{\varphi}_r\right)\right]^{(\boldsymbol{\varphi}_r)}+\left(\boldsymbol{\varphi}_r^T\mathbf{A}_{r,i}\boldsymbol{\varphi}_r\right)\left(\mathbf{B}_i\boldsymbol{\varphi}_r\right)\left[\left(\boldsymbol{\varphi}_r^T\mathbf{B}_i\boldsymbol{\varphi}_r\right)^{-2}\right]^{(\boldsymbol{\varphi}_r)} \\
&=\left(\boldsymbol{\varphi}_r^T\mathbf{B}_i\boldsymbol{\varphi}_r\right)^{-2}\left[\left(\boldsymbol{\varphi}_r^T\mathbf{A}_{r,i}\boldsymbol{\varphi}_r\right)\mathbf{B}_i+2\left(\mathbf{B}_i\boldsymbol{\varphi}_r\right)\left(\boldsymbol{\varphi}_r^T\mathbf{A}_{r,i}\right)\right]+\left(\boldsymbol{\varphi}_r^T\mathbf{A}_{r,i}\boldsymbol{\varphi}_r\right)\left(\mathbf{B}_i\boldsymbol{\varphi}_r\right)\left[-2\left(\boldsymbol{\varphi}_r^T\mathbf{B}_i\boldsymbol{\varphi}_r\right)^{-3}\left(2\boldsymbol{\varphi}_r^T\mathbf{B}_i\right)\right] \\
&=\left(\boldsymbol{\varphi}_r^T\mathbf{B}_i\boldsymbol{\varphi}_r\right)^{-2}\left[\left(\boldsymbol{\varphi}_r^T\mathbf{A}_{r,i}\boldsymbol{\varphi}_r\right)\mathbf{B}_i+2\left(\mathbf{B}_i\boldsymbol{\varphi}_r\right)\left(\boldsymbol{\varphi}_r^T\mathbf{A}_{r,i}\right)\right]-4\left(\boldsymbol{\varphi}_r^T\mathbf{A}_{r,i}\boldsymbol{\varphi}_r\right)\left(\boldsymbol{\varphi}_r^T\mathbf{B}_i\boldsymbol{\varphi}_r\right)^{-3}\left(\mathbf{B}_i\boldsymbol{\varphi}_r\boldsymbol{\varphi}_r^T\mathbf{B}_i\right)
\end{aligned}
\tag{A5a}
$$

$$
\begin{aligned}
\left[\left(\boldsymbol{\varphi}_r^T\mathbf{B}_i\boldsymbol{\varphi}_r\right)^{-1}\left(\mathbf{A}_{r,i}\boldsymbol{\varphi}_r\right)\right]^{(\boldsymbol{\varphi}_r)} &=\left(\boldsymbol{\varphi}_r^T\mathbf{B}_i\boldsymbol{\varphi}_r\right)^{-1}\left(\mathbf{A}_{r,i}\boldsymbol{\varphi}_r\right)^{(\boldsymbol{\varphi}_r)}+\left(\mathbf{A}_{r,i}\boldsymbol{\varphi}_r\right)\left[\left(\boldsymbol{\varphi}_r^T\mathbf{B}_i\boldsymbol{\varphi}_r\right)^{-1}\right]^{(\boldsymbol{\varphi}_r)} \\
&=\left(\boldsymbol{\varphi}_r^T\mathbf{B}_i\boldsymbol{\varphi}_r\right)^{-1}\mathbf{A}_{r,i}+\left(\mathbf{A}_{r,i}\boldsymbol{\varphi}_r\right)\left[-2\left(\boldsymbol{\varphi}_r^T\mathbf{B}_i\boldsymbol{\varphi}_r\right)^{-2}\left(\boldsymbol{\varphi}_r^T\mathbf{B}_i\right)\right] \\
&=\left(\boldsymbol{\varphi}_r^T\mathbf{B}_i\boldsymbol{\varphi}_r\right)^{-1}\mathbf{A}_{r,i}-2\left(\boldsymbol{\varphi}_r^T\mathbf{B}_i\boldsymbol{\varphi}_r\right)^{-2}\left(\mathbf{A}_{r,i}\boldsymbol{\varphi}_r\boldsymbol{\varphi}_r^T\mathbf{B}_i\right)
\end{aligned}
\tag{A6b}
$$

$$
\begin{aligned}
&\left[\left(\boldsymbol{\varphi}_r^T\mathbf{B}_i\boldsymbol{\varphi}_r\right)^{-3/2}\left(\boldsymbol{\eta}_{r,i}^T\boldsymbol{\varphi}_r\right)\left(\mathbf{B}_i\boldsymbol{\varphi}_r\right)\right]^{(\boldsymbol{\varphi}_r)} \\
&=\left(\boldsymbol{\varphi}_r^T\mathbf{B}_i\boldsymbol{\varphi}_r\right)^{-3/2}\left[\left(\boldsymbol{\beta}_{r,i}^T\boldsymbol{\varphi}_r\right)\left(\mathbf{B}_i\boldsymbol{\varphi}_r\right)\right]^{(\boldsymbol{\varphi}_r)}+\left(\boldsymbol{\eta}_{r,i}^T\boldsymbol{\varphi}_r\right)\left(\mathbf{B}_i\boldsymbol{\varphi}_r\right)\left[\left(\boldsymbol{\varphi}_r^T\mathbf{B}_i\boldsymbol{\varphi}_r\right)^{-3/2}\right]^{(\boldsymbol{\varphi}_r)} \\
&=\left(\boldsymbol{\varphi}_r^T\mathbf{B}_i\boldsymbol{\varphi}_r\right)^{-3/2}\left[\left(\boldsymbol{\eta}_{r,i}^T\boldsymbol{\varphi}_r\right)\mathbf{B}_i+\left(\mathbf{B}_i\boldsymbol{\varphi}_r\right)\boldsymbol{\eta}_{r,i}^T\right]+\left(\boldsymbol{\eta}_{r,i}^T\boldsymbol{\varphi}_r\right)\left(\mathbf{B}_i\boldsymbol{\varphi}_r\right)\left[-3\left(\boldsymbol{\varphi}_r^T\mathbf{B}_i\boldsymbol{\varphi}_r\right)^{-5/2}\left(\boldsymbol{\varphi}_r^T\mathbf{B}_i\right)\right] \\
&=\left(\boldsymbol{\varphi}_r^T\mathbf{B}_i\boldsymbol{\varphi}_r\right)^{-3/2}\left[\left(\boldsymbol{\eta}_{r,i}^T\boldsymbol{\varphi}_r\right)\mathbf{B}_i+\left(\mathbf{B}_i\boldsymbol{\varphi}_r\right)\boldsymbol{\eta}_{r,i}^T\right]-3\left(\boldsymbol{\eta}_{r,i}^T\boldsymbol{\varphi}_r\right)\left(\boldsymbol{\varphi}_r^T\mathbf{B}_i\boldsymbol{\varphi}_r\right)^{-5/2}\left(\mathbf{B}_i\boldsymbol{\varphi}_r\boldsymbol{\varphi}_r^T\mathbf{B}_i\right)
\end{aligned}
\tag{A6c}
$$

$$
\begin{aligned}
\left[\left(\boldsymbol{\varphi}_r^T\mathbf{B}_i\boldsymbol{\varphi}_r\right)^{-1/2}\boldsymbol{\eta}_{r,i}\right]^{(\boldsymbol{\varphi}_r)} &=\boldsymbol{\eta}_{r,i}\left[-\left(\boldsymbol{\varphi}_r^T\mathbf{B}_i\boldsymbol{\varphi}_r\right)^{-3/2}\left(\boldsymbol{\varphi}_r^T\mathbf{B}_i\right)\right] \\
&=-\left(\boldsymbol{\varphi}_r^T\mathbf{B}_i\boldsymbol{\varphi}_r\right)^{-3/2}\left(\boldsymbol{\eta}_{r,i}\boldsymbol{\varphi}_r^T\mathbf{B}_i\right)
\end{aligned}
\tag{A6d}
$$

Substituting Eqs. (A6a)-(A6d) into (A5) leads to

$$
\begin{aligned}
L_{as}^{(\boldsymbol{\varphi}_r\boldsymbol{\varphi}_r)} &= \sum_{i=1}^{n_t} \left\{ \begin{array}{l} \left(\boldsymbol{\varphi}_r^T \mathbf{B}_i \boldsymbol{\varphi}_r\right)^{-2} \left[ -\left(\boldsymbol{\varphi}_r^T \mathbf{A}_{r,i} \boldsymbol{\varphi}_r\right) \mathbf{B}_i - 2\left(\mathbf{B}_i \boldsymbol{\varphi}_r\right)\left(\boldsymbol{\varphi}_r^T \mathbf{A}_{r,i}\right) - 2\left(\mathbf{A}_{r,i} \boldsymbol{\varphi}_r\right)\left(\boldsymbol{\varphi}_r^T \mathbf{B}_i\right) \right] + \left(\boldsymbol{\varphi}_r^T \mathbf{B}_i \boldsymbol{\varphi}_r\right)^{-1} \mathbf{A}_{r,i} + \\ 4\left(\boldsymbol{\varphi}_r^T \mathbf{B}_i \boldsymbol{\varphi}_r\right)^{-3} \left(\boldsymbol{\varphi}_r^T \mathbf{A}_{r,i} \boldsymbol{\varphi}_r\right)\left(\mathbf{B}_i \boldsymbol{\varphi}_r \boldsymbol{\varphi}_r^T \mathbf{B}_i\right) + \left(\boldsymbol{\varphi}_r^T \mathbf{B}_i \boldsymbol{\varphi}_r\right)^{-3/2} \left[ \left(\boldsymbol{\eta}_{r,i}^T \boldsymbol{\varphi}_r\right) \mathbf{B}_i + \left(\mathbf{B}_i \boldsymbol{\varphi}_r \boldsymbol{\eta}_{r,i}^T\right) + \left(\boldsymbol{\eta}_{r,i} \boldsymbol{\varphi}_r^T \mathbf{B}_i\right) \right] \\ -3\left(\boldsymbol{\varphi}_r^T \mathbf{B}_i \boldsymbol{\varphi}_r\right)^{-5/2} \left(\boldsymbol{\eta}_{r,i}^T \boldsymbol{\varphi}_r\right)\left(\mathbf{B}_i \boldsymbol{\varphi}_r \boldsymbol{\varphi}_r^T \mathbf{B}_i\right) \end{array} \right\} \\
&= \sum_{i=1}^{n_t} \left[ \left(\boldsymbol{\varphi}_r^T \mathbf{B}_i \boldsymbol{\varphi}_r\right)^{-3} \left\{ \begin{array}{l} \left(\boldsymbol{\varphi}_r^T \mathbf{B}_i \boldsymbol{\varphi}_r\right) \left[ -\left(\boldsymbol{\varphi}_r^T \mathbf{A}_{r,i} \boldsymbol{\varphi}_r\right) \mathbf{B}_i - 4\left(\mathbf{B}_i \boldsymbol{\varphi}_r\right)\left(\boldsymbol{\varphi}_r^T \mathbf{A}_{r,i}\right) \right] + \left(\boldsymbol{\varphi}_r^T \mathbf{B}_i \boldsymbol{\varphi}_r\right)^{2} \mathbf{A}_{r,i} + \\ 4\left(\boldsymbol{\varphi}_r^T \mathbf{A}_{r,i} \boldsymbol{\varphi}_r\right)\left(\mathbf{B}_i \boldsymbol{\varphi}_r \boldsymbol{\varphi}_r^T \mathbf{B}_i\right) + \left(\boldsymbol{\varphi}_r^T \mathbf{B}_i \boldsymbol{\varphi}_r\right)^{3/2} \left[ \left(\boldsymbol{\eta}_{r,i}^T \boldsymbol{\varphi}_r\right) \mathbf{B}_i + 2\left(\mathbf{B}_i \boldsymbol{\varphi}_r \boldsymbol{\eta}_{r,i}^T\right) \right] \\ -3\left(\boldsymbol{\varphi}_r^T \mathbf{B}_i \boldsymbol{\varphi}_r\right)^{1/2} \left(\boldsymbol{\eta}_{r,i}^T \boldsymbol{\varphi}_r\right)\left(\mathbf{B}_i \boldsymbol{\varphi}_r \boldsymbol{\varphi}_r^T \mathbf{B}_i\right) \end{array} \right\} \right]
\end{aligned}
\tag{A7}
$$

## Appendix II: Connecting $\nu_{r,i}$ (the 'noise-to-environment' ratio confined to $i$-th setup) with $\nu_{r,all}$ (the 'noise-to-environment' ratio confined to all sensors)

The PSD of modal excitation is dependent on mode shape, which arises from the relationship between the physical and modal response, and the scaling of the mode shape. Here the theory derived in [39] will be used to connect $\nu_{r,i}$ with $\nu_{r,all}$. Based on the standard structural dynamics, one can figure out that the PSD of modal force $S_p$ is given by [39]

$$
S_p = \frac{\boldsymbol{\Phi}_r^T \mathbf{S}_\mathbf{F} \boldsymbol{\Phi}_r}{\left(\boldsymbol{\Phi}_r^T \mathbf{M} \boldsymbol{\Phi}\right)^2} \tag{A8}
$$

where $\mathbf{M}$ is the mass matrix, $\mathbf{S}_\mathbf{F}$ is the PSD matrix of the forces applied on the structure and $\boldsymbol{\Phi}=\{\Phi_1,\cdots,\Phi_{n_i},\cdots,\ \Phi_{n_t}\}$ is the true 'full' mode shape containing all dofs of the structure concerned. The PSD of modal force $S_{f,r,i}$ identified from the $i$-th setup is proportional to the sum of squares of the mode shape values at the measured dofs, i.e. [39]

$$
S_{f,r,i} = S_p \sum_{j=1}^{n_i} \Phi_j^2 \tag{A9}
$$

Here $\Phi_j\left(j=1,2,\cdots,n_i\right)$ denote the vector involving the elements of $\boldsymbol{\Phi}$ corresponding to the dofs of the $i$-th setup. It can be reasoned that if $\Phi_{n_i}$ is scaled down (i.e., divided) by a factor then

$S_{f,r,i}$ should be scaled up (i.e., multiplied) by the square of that factor. This equation shows that $S_{f,r,i}$ is proportional to the sum of squares of the mode shape values at the measured dofs. Note that the equation only provides a conceptual understanding, and it is not useful for computing $S_{f,r,i}$ because $S_p$ is not available in reality.

Similarly, the modal excitation PSD $S_{f,r,all}$ identified from all $n_l$ measured dofs should be scaled by $\sum_{j=1}^{n_l}\Phi_j^2$, i.e.

$$S_{f,r,all} = S_p \sum_{j=1}^{n_l}\Phi_j^2 \tag{A10}$$

Combing (A9) and (A10), one can obtain that

$$\frac{S_{f,r,i}}{\sum_{j=1}^{n_i}\Phi_j^2} = \frac{S_{f,r,all}}{\sum_{j=1}^{n_l}\Phi_j^2} \tag{A11}$$

From (A11), one can figure out that $S_{f,r,i}$ satisfies:

$$S_{f,r,i} = \frac{\sum_{j=1}^{n_i}\Phi_j^2}{\sum_{j=1}^{n_l}\Phi_j^2} S_{f,r,all} \tag{A12}$$

It is not difficult to figure out that that

$$\frac{\sum_{j=1}^{n_i}\Phi_j^2}{\sum_{j=1}^{n_l}\Phi_j^2} \approx \frac{\boldsymbol{\varphi}_r^T \mathbf{B}_i \boldsymbol{\varphi}_r}{\boldsymbol{\varphi}_r^T \boldsymbol{\varphi}_r} = \boldsymbol{\varphi}_r^T \mathbf{B}_i \boldsymbol{\varphi}_r \tag{A13}$$

Substituting (A13) into (A12), the 'noise-to-environment' ratio corresponding to the $i$-th setup can be estimated as

$$\nu_{r,i} = \frac{S_{\mu,r,i}}{S_{f,r,i}} \approx \frac{S_{\mu,r,all}}{\left(\boldsymbol{\varphi}_r^T \mathbf{B}_i \boldsymbol{\varphi}_r\right) S_{f,r,all}} = \left(\boldsymbol{\varphi}_r^T \mathbf{B}_i \boldsymbol{\varphi}_r\right)^{-1} \nu_{r,all} \tag{A14}$$

## References


[1] W.J. Yan, L.S. Katafygiotis, A two-stage fast Bayesian spectral density approach for ambient modal analysis. Part II: mode shape assembly and case studies, Mechanical System and Signal Processing 54 (2015) 156-171.

[2] S.K. Au, Assembling mode shapes by least squares, Mechanical Systems and Signal Processing 25(1) (2011) 163-179.

[3] S.K. Au, F.L. Zhang, Fast Bayesian ambient modal identification incorporating multiple setups. Journal of Engineering Mechanics 138(7) (2012) 800-815.

[4] W.J. Yan, W.X. Ren, Operational modal parameter identification from power spectrum density transmissibility, Computer-Aided Civil and Infrastructure Engineering 27(3) (2012) 202-217.

[5] W.J. Yan, W.X. Ren, An Enhanced Power Spectral Density Transmissibility (EPSDT) approach for operational modal analysis: Theoretical and experimental investigation. Engineering Structures 2015; 102: 108-119.

[6] J.X. Mao, H. Wang, D.M. Feng, T.Y. Tao, W.Z. Zheng, Investigation of dynamic properties of long‐span cable‐stayed bridges based on one‐year monitoring data under normal operating condition. Structural Control and Health Monitoring 25(5) (2018) e2146.

[7] N. Martins, E. Caetano, S. Diord, F. Magalhães, Á. Cunha. Dynamic monitoring of a stadium suspension roof: Wind and temperature influence on modal parameters and structural response, Engineering Structures 59 (2014) 80-94.

[8] G. Tondreau, A. Deraemaeker, Numerical and experimental analysis of uncertainty on modal parameters estimated with the stochastic subspace method, Journal of Sound and Vibration 333(18) (2014) 4376-401.

[9] R. Pintelon, P. Guillaume, J. Schoukens, Uncertainty calculation in (operational) modal analysis, Mechanical Systems and Signal Processing 21(6) (2007) 2359-2373.

[10] M. El-kafafy, T. De Troyer, B. Peeters, P. Guillaume, Fast maximum-likelihood identification of modal parameters with uncertainty intervals: a modal model-based formulation, Mechanical Systems and Signal Processing 37(1-2) (2013) 422-439.

[11] M. El-Kafafy, B. Peeters, P. Guillaume, T. De Troyer, Constrained maximum likelihood modal parameter identification applied to structural dynamics, Mechanical Systems and Signal Processing 72 (2016) 567-589.

[12] E. Reynders, R. Pintelon, G. De Roeck, Uncertainty bounds on modal parameters obtained from stochastic subspace identification, Mechanical Systems and Signal Processing 22(4) (2008) 948-969.

[13] E. Reynders, K. Maes, G. Lombaert, G. De Roeck, Uncertainty quantification in operational modal analysis with stochastic subspace identification: validation and applications, Mechanical Systems and Signal Processing 66 (2016) 13-30.

[14] M. Döhler, X.B. Lam, L. Mevel, Uncertainty quantification for modal parameters from stochastic subspace identification on multi-setup measurements, Mechanical Systems and Signal Processing 36(2) (2013) 562-581.

[15] M. Döhler, L. Mevel, Efficient multi-order uncertainty computation for stochastic subspace identification, Mechanical Systems and Signal Processing 38(2) (2013) 346-366.

[16] J.L. Beck, Bayesian system identification based on probability logic, Structural Control and Health Monitoring 17 (2010) 825-847.

[17] J.L. Beck, L.S. Katafygiotis, Updating models and their uncertainties. I: Bayesian statistical framework, Journal of Engineering Mechanics, ASCE 124(4) (1998) 455-461.

[18] L.S. Katafygiotis, H.F. Lam, C. Papadimitriou, Treatment of unidentifiability in structural model updating, Advances in Structural Engineering 3(1) (2000) 19-39.

[19] J.Y. Ching, M. Muto, J.L. Beck, Structural model updating and health monitoring with incomplete modal data using Gibbs sampler, Computer-Aided Civil and Infrastructure Engineering 21(4) (2006) 242-257.

[20] K.V. Yuen, J.L. Beck, L.S. Katafygiotis, Efficient model updating and monitoring methodology using incomplete modal data without mode matching, Structural Control and Health Monitoring 13(1) (2006) 91-107.

[21] C. Papadimitriou, D.C. Papadioti, Component mode synthesis techniques for finite element model updating, Computers and Structures 126 (2013)15-28.

[22] W.J. Yan, L.S. Katafygiotis, A novel Bayesian approach for structural model updating utilizing statistical modal information from multiple setups, Structural Safety 52 (2015) 260-271.

[23] H.F. Lam, C.T. Ng, A probabilistic method for the detection of obstructed cracks of beam-type structures using spatial wavelet transform, Probabilistic Engineering Mechanics 23(2-3) (2008) 237-45.
[24] C. Papadimitriou, J.L. Beck, L.S. Katafygiotis, Updating robust reliability using structural test data, Probabilistic Engineering Mechanics 16(2) (2001) 103-113.
[25] H.A. Jensen, C. Vergara, C. Papadimitriou, The use of updated robust reliability measures in stochastic dynamical systems, Computer Methods in Applied Mechanics and Engineering 267(2013) 293-317.
[26] J.L. Beck, K.V. Yuen, Model selection using response measurements: Bayesian probabilistic approach, Journal of Engineering Mechanics, ASCE 130(2) (2004) 192-203.
[27] K.V. Yuen, Recent developments of Bayesian model class selection and applications in civil engineering, Structural Safety 32(5) (2010) 338-46.
[28] K.V. Yuen, L.S. Katafygiotis, Bayesian fast Fourier transform approach for modal updating using ambient data, Advance in Structural Engineering 6(2) (2003) 81-95.
[29] K.V. Yuen, L.S. Katafygiotis, Bayesian time-domain approach for modal updating using ambient data, Probabilistic Engineering Mechanics 16(3) (2001) 219-231.
[30] L.S. Katafygiotis, K.V. Yuen, Bayesian spectral density approach for modal updating using ambient data, Earthquake Engineering and Structural Dynamics 30(8) (2001) 1103-1112.
[31] S.K. Au, Fast Bayesian FFT method for ambient modal identification with separated modes, Journal of Engineering Mechanics, ASCE 137(3) (2011) 214-226.

[32] S.K. Au, Fast Bayesian ambient modal identification in the frequency domain, Part I: posterior most probable value, Mechanical Systems and Signal Processing 26(1) (2012) 60-75.

[33] W.J. Yan, L.S. Katafygiotis, A two-stage fast Bayesian spectral density approach for ambient modal analysis. Part I: posterior most probable value and uncertainty. Mechanical System and Signal Processing 54 (2015)139-155.

[34] W.J. Yan, M.Y. Zhao, Q. Sun, W.X. Ren, Transmissibility-based system identification for structural health Monitoring: Fundamentals, approaches, and applications. Mechanical Systems and Signal Processing 117 (2019) 453-82.

[35] H.F. Lam, J. Hu, J.H. Yang, Bayesian operational modal analysis and Markov chain Monte Carlo-based model updating of a factory building, Engineering Structures 132 (2017) 314-336.

[36] J.M.W. Brownjohn, S.K. Au, Y. Zhu, Z. Sun, B. Li, J. Bassitt, E. Hudson, H. Sun, Bayesian operational modal analysis of Jiangyin Yangtze River Bridge, Mechanical Systems and Signal Processing, 110 (2018) 210-230.

[37] F.L. Zhang, S.K. Au, H.F. Lam, Assessing uncertainty in operational modal analysis incorporating multiple setups using a Bayesian approach, Structural Control and Health Monitoring, 22(3) (2015) 395-416.

[38] S.K. Au, Uncertainty law in ambient modal identification. Part I: Theory, Mechanical Systems and Signal Processing 48(1) (2014)15-33.

[39] S.K. Au, Uncertainty law in ambient modal identification. Part II: Implication and field verification, Mechanical Systems and Signal Processing 48(1) (2014) 34-48.

[40] W.J. Yan, L.S. Katafygiotis, An analytical investigation into the propagation properties of uncertainty in a two-stage fast Bayesian spectral density approach for ambient modal analysis, Mechanical Systems and Signal Processing 118 (2019) 503-533.

[41] S.K. Au, F.L. Zhang, On assessing the posterior mode shape uncertainty in ambient modal identification, Probabilistic Engineering Mechanics 26(3) (2011) 427-434.

[42] C. Papadimitriou, J.L. Beck, S.K. Au, Entropy-based optimal sensor location for structural model updating, Journal of Vibration and Control 6(5) (2000) 781-800.

[43] K.V. Yuen, S.C. Kuok, Efficient Bayesian sensor placement algorithm for structural identification: a general approach for multi-type sensory systems, Earthquake Engineering and Structural Dynamics, 44(5) (2015) 757-774.

[44] C. Papadimitriou, Optimal sensor placement methodology for parametric identification of structural systems, Journal of sound and vibration 278(4-5) (2004) 923-47.

[45] C. Argyris, Bayesian uncertainty quantification and optimal experimental design in data-driven simulations of engineering systems, PhD thesis, University of Thessaly, 2017.

[46] C. Papadimitriou, C. Argyris, D.C. Papadioti, P. Panetsos, Uncertainty calibration of large-order models of bridges using ambient vibration measurements, In EWSHM-7th European Workshop on Structural Health Monitoring, July, 2014, Nantes, France.

## Table Captions

- Table 1: Setup information for the shear building
- Table 2. Identified spectrum variables of the numerical study
- Table 3. Measurement setups of the Metsovo Bridge
- Table 4. Identified spectrum variables of the Metsovo Bridge with $\kappa = 6$

# Figure Captions

- Fig. 1: Common architecture for operational modal test with multiple setups
- Fig. 2: The data length factor for the mode shape
- Fig. 3: The optimal values (square) and two times standard deviation (asterisk) of the assembled global mode shapes (numerical study)
- Fig. 4: Comparison of the overall uncertainty of the global mode shapes with ‘exact’ method denoted by markers and ‘approximate’ method denoted by solid lines versus bandwidth factor (numerical study)
- Fig. 5: Comparison of the overall uncertainty of the global mode shapes with ‘exact’ method denoted by markers and ‘approximate’ method denoted by solid lines versus noise level (numerical study)
- Fig. 6: The sideview of the Metsovo bridge
- Fig. 7: Experimental setups of ambient vibration test for the Metsovo bridge
- Fig. 8: Sensor configuration for the ambient vibration test of the Metsovo bridge
- Fig. 9: PSD of the accelerations in the transverse direction and vertical direction
- Fig. 10: Comparison between the experimentally identified (left column) and nominal FE model predicted (right column) transverse bending mode shapes of the Metsovo bridge
- Fig. 11: Comparison between the experimentally identified (left column) and nominal FE model predicted (right column) vertical bending mode shapes of the Metsovo bridge
- Fig. 12: Posterior overall uncertainty of the assembled global mode shapes versus bandwidth factor (experimental study): the ‘exact’ values are denoted by markers and the ‘approximate’ values are represented by solid lines
- Fig. 13: Posterior overall uncertainty of the assembled global mode shapes versus time duration (experimental study): the ‘exact’ values are denoted by markers and the ‘approximate’ values are represented by solid lines